J. Phys. B: At. Mol. Opt. Phys. **32** (1999) 2801–2829. Printed in the UK PII: S0953-4075(99)96659-2

# Elastic electron scattering by laser-excited $^{138}$Ba( . . . 6s6p $^1$P$_1$) atoms

S Trajmar†‡, I Kanik†§, M A Khakoo§, L R LeClair†[+], I Bray‖, D Fursa‖ and G Csanak¶

† California Institute of Technology, Jet Propulsion Laboratory, Pasadena, CA 91109, USA
‡ California Institute of Technology, Division of Chemistry and Chemical Engineering, Pasadena, CA 91109, USA
§ California State University, Department of Physics, Fullerton, CA 92834, USA
‖ Electronic Structure of Materials Centre, The Flinders University of South Australia, GPO Box 2100, Adelaide 5001, Australia
¶ University of California, Los Alamos National Laboratory, Los Alamos, NM 87544, USA

Received 10 August 1998, in final form 22 February 1999

**Abstract.** The results of a joint experimental and theoretical study concerning elastic electron scattering by laser-excited $^{138}$Ba(. . . 6s6p $^1$P$_1$) atoms are described. These studies demonstrate several important aspects of elastic electron collisions with coherently excited atoms, and are the first such studies. From the measurements, collision and coherence parameters, as well as cross sections associated with an atomic ensemble prepared with an arbitrary in-plane laser geometry and linear polarization (with respect to the collision frame), or equivalently with any magnetic sublevel superposition, have been obtained at 20 eV impact energy and at 10°, 15° and 20° scattering angles. The convergent close-coupling (CCC) method was used within the non-relativistic $LS$-coupling framework to calculate the magnetic sublevel scattering amplitudes. From these amplitudes all the parameters and cross sections at 20 eV impact energy were extracted in the full angular range in 1° steps. The experimental and theoretical results were found to be in good agreement, indicating that the CCC method can be reliably applied to elastic scattering by $^{138}$Ba(. . . 6s6p $^1$P$_1$) atoms, and possibly to other heavy elements when spin–orbit coupling effects are negligible. Small but significant asymmetry was observed in the cross sections for scattering to the left and to the right. It was also found that elastic electron scattering by the initially isotropic atomic ensemble resulted in the creation of significant alignment. As a byproduct of the present studies, elastic scattering cross sections for metastable $^{138}$Ba atoms were also obtained.

## 1. Introduction

A large body of electron collision cross section data exists for various ground state atomic and molecular species. However, the same cannot be said regarding excited species. This is mainly due to the difficulties in generating these species in suitably high concentrations for electron scattering measurements. The various methods for preparing excited atoms and the available electron collision cross section data for these atoms have been summarized by Lin and Anderson (1992), and by Trajmar and Nickel (1992). With the introduction of lasers for the preparation of the excited atoms many of the difficulties encountered earlier have been surmounted but certain new aspects, such as coherence and polarization, have entered the electron excitation process. The first application of laser excitation in electron scattering measurements was introduced in

[+] Present address: MPB Technologies, Pointe Claire, Quebec H9R 4R8, Canada.

0953-4075/99/122801+29$19.50  

the early 1970s by Hertel and co-workers for Na (see, e.g., Hertel and Stoll 1974a, b, 1977). Shortly thereafter similar studies on Ba (see, e.g., Register *et al* 1978, 1983) were initiated in our laboratory. Measurements have been reported subsequently on Na (Herman and Hertel 1982, McClelland *et al* 1992, Scholten *et al* 1993, Sang *et al* 1994, Hall *et al* 1996), Ba (Zetner *et al* 1990, 1993, Li and Zetner 1994a, 1995, 1996), Ca (Law and Teubner 1995, Teubner *et al* 1996), Li (Karagonov *et al* 1996, Teubner *et al* 1996), Rb (Hall *et al* 1996), Cr (Hanne *et al* 1993) and Yb (Li and Zetner 1994b). In these studies the superelastic scattering signal corresponding to the electron-impact de-excitation of the laser-prepared state to the ground state was measured as a function of the laser geometry and polarization (with respect to the collision frame). The results were then interpreted in terms of the electron-impact coherence parameters (EICPs) characterizing the state prepared in the hypothetical inverse-inelastic scattering process. This hypothetical inverse process corresponds to electron-impact excitation of the isotropic, incoherent ground state to the upper state. The interpretation is based on the theory of Macek and Hertel (1974). The EICPs fully characterize the state produced by the electron-impact excitation, including its polarization and coherence properties. These enable us to obtain a deeper insight into the nature of electron–atom interactions and serve as more rigorous checks on theoretical methods than cross sections derived from conventional scattering measurements. Some results have also been reported for stepwise excitation processes, e.g. inelastic scattering by laser-excited atoms (Hermann *et al* 1977, Masters *et al* 1996, Zetner *et al* 1997). The results of all of these studies have been extensively discussed in the literature and at the *Coherence and Correlation Symposia* associated with the *International Conference on the Physics of Electronic and Atomic Collisions*. However, no studies similar to the superelastic and stepwise excitation measurements have been reported for *elastic* scattering by laser-excited atoms.

The purpose of the present paper is to describe the results of a joint experimental and theoretical study concerning *elastic* electron scattering by laser-excited $^{138}\mathrm{Ba}\left(\ldots 6s6p\ ^1\mathrm{P}_1\right)$ atoms. The motivation for this work was: the absence of this type of data, the need to check the applicability of the convergent close-coupling (CCC) method to electron scattering calculations involving heavy and excited atoms and the question and contrary views raised in connection with plasma polarization spectroscopy as to whether elastic scattering by initially isotropic atoms can create alignment and to what degree (Petrashen *et al* 1983, Dashevskaya and Nikitin 1987, Fujimoto 1996, Kazantsev 1996). A brief discussion of this work was published previously (Trajmar *et al* 1998). In the present paper we give a more detailed description of the experimental and data interpretation procedures as well as additional theoretical results.

It should be mentioned for completeness that Vuskovic and co-workers (Zuo *et al* 1990, Shi *et al* 1996, Vuskovic 1996) deduced certain elastic and inelastic electron scattering cross sections for oriented $\mathrm{Na}\left(3\,^2\mathrm{P}_{3/2},\ F=3,\ M_F=\pm 3\right)$ atoms from atomic recoil measurements.

## 2. Experimental

### *2.1. Experimental arrangements*

Figure 1 shows schematically the experimental arrangement. A nearly monoenergetic electron beam (full-width at half-maximum of about 50 meV) with initial momentum vector $\vec{k}_i$ crosses a Ba beam at a 90° angle. Electrons scattered by the polar angles $\theta$ and $\phi$ (with respect to the laboratory frame) with final momentum vector $\vec{k}_f$ are detected over a small solid angle ($\Delta\Omega \sim 10^{-3}$ sr). The spins of the incoming and scattered electrons are not determined in the present experiments. The scattering plane is defined by $\vec{k}_i$ and $\vec{k}_f$ and the fixed laboratory

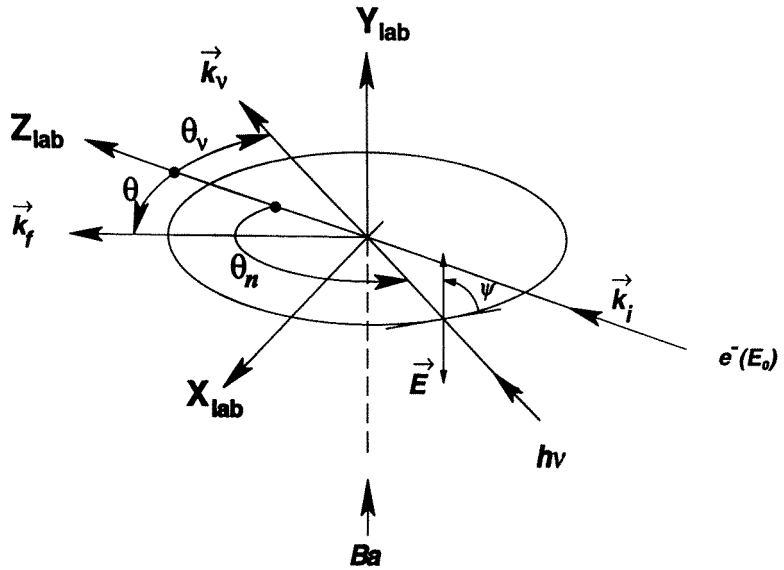


**Figure 1.** Schematic experimental arrangement. The laboratory coordinate system, the laser beam, the polar angles for the forward process (with respect to $Z_{\rm coll}$ which is the same as $Z_{\rm lab}$) and the polarization angle are shown.

coordinate system is indicated in the figure. $Z_{\rm lab}$ lies along $\vec{k}_i$, $X_{\rm lab}$ is in the scattering plane and on the same side of $\vec{k}_i$ as the laser, and $Y_{\rm lab}$ together with $X_{\rm lab}$ and $Z_{\rm lab}$ forms a right-handed coordinate system. The Ba beam propagates along the $Y_{\rm lab}$-axis. It is collimated with an aspect ratio of about 10 and contains all the isotopes in their naturally occurring ratios. We will be concerned here mainly with the 138 isotope which constitutes about 72% of the beam. The laser beam is located *in the scattering plane* and the polar coordinates of its direction ($\vec{k}_v$) with respect to the laboratory coordinate system are denoted by $\theta_v$ and $\phi_v$ (which was always 180°). We will refer to this laser arrangement as *laser centre* (C). We define a collision coordinate system for which the $Z_{\rm coll}$-axis lies along the momentum of the incoming electron, the $X_{\rm coll}$-axis is in the scattering plane in such a way that the azimuthal scattering angle $\phi_{\rm coll}$ is always zero, and the $Y$-axis is chosen to form a right-handed coordinate system. We will define a collision frame both for the actual experimental 'forward' scattering process and for the hypothetical 'inverse' scattering process. We also introduce the laser frame with the $Z$-axis, $Z_{\rm ph'}$ along $-\vec{k}_v$ and denote the polar coordinate of $Z_{\rm ph'}$ with respect to the collision frame by $\theta_n, \phi_n$. Later, we will define the relations between the two sets of laser polar angles. For a detailed description of the coordinate systems, see Zetner *et al* (1990). The laser beam is linearly polarized, and the angle of polarization with respect to the scattering plane is denoted as $\psi$. The laser beam was produced by a tunable single-mode ring-dye laser which was tuned to excite the $\left(6s^2\ {}^1S_0 \rightarrow 6s6p\ {}^1P_1\right)$ transition in $^{138}$Ba. In some measurements the laser was moved below the scattering plane (upstream of the Ba beam). We will refer to this arrangement as *laser low* (L).

The laser and barium beams can be chopped (on/off) by computer control, which also controls the operation of the multichannel scaler and data handling. The sweep voltage, required for the energy-loss scan, was generated by a digital-to-analogue converter which produced a voltage proportional to the channel number being addressed in the multichannel

scaler. The polarization angle of the laser light could be continuously rotated under computer control and the signal corresponding to the angular range $\psi = 90^\circ$–$690^\circ$ was recorded in a multichannel scaling mode. During the measurements the fluorescence signal from the laser-excited section of the Ba beam was also continuously recorded in order to monitor the laser pumping conditions. Details concerning the electron gun and detectors, the Ba and laser beam sources and other experimental aspects have been described previously (Register *et al* 1983, Trajmar and Register 1984, Zetner *et al* 1990).

### *2.2. Measurement procedures*

With the arrangements described above, three types of measurements were carried out:

(a) The scattering intensity as a function of energy lost by the electron ($\Delta E$) was measured at a fixed impact energy ($E_0$), scattering angle ($\theta$), laser geometry ($\theta_n, \phi_n$) and laser polarization $\psi$. The results of these measurements are energy-loss spectra.

(b) The scattering intensity was measured at fixed laser geometries and $E_0, \theta$ values in a given energy-loss channel (fixed $\Delta E$) as a function of the laser beam polarization. Here, we measured the scattering signal from atomic ensembles possessing various degrees of coherence and alignment in their magnetic sublevels. The results of these measurements are the intensity modulation curves.

(c) Auxiliary measurements (check measurements) of scattering intensities in the $\left({}^1\mathrm{S}_0\text{–}{}^1\mathrm{P}_1\right)$ inelastic, the $\left({}^1\mathrm{P}_1\text{–}{}^1\mathrm{S}_0\right)$ superelastic and the various elastic channels with fixed $E_0, \theta, \theta_n, \phi_n, \psi$ were carried out to monitor the electron scattering conditions and to enable the background subtraction, the separation of the signals associated with various elastic scattering channels, and also the normalization of the intensities to the corresponding cross sections.

The elastic scattering signal was a superposition of scattering by all species present in the beam plus the background. When the laser was turned off, all isotopes in the Ba beam were present in their ground state. With the laser-centre arrangement, we had Ba atoms of all isotopes in their ground state plus the laser-excited ${}^1\mathrm{P}_1$ and the cascade populated metastable (mainly ${}^1\mathrm{D}_2$ and ${}^3\mathrm{D}_2$) species of ${}^{138}$Ba. With the laser-low arrangement, the situation was the same as for the laser-centre arrangement except that the ${}^1\mathrm{P}_1$ species were missing because they decayed by spontaneous emission to the underlying levels by the time the atoms reached the region where the electron beam intersected the Ba beam. In these energy-loss spectra, the features to the right-hand side of the elastic peak correspond to the various inelastic (ground–excited or excited–excited) transition processes, whereas features on the left-hand side of the elastic peak represent superelastic (energy gain) scattering processes.

A typical intensity modulation curve for the $\left({}^1\mathrm{S}_0\text{–}{}^1\mathrm{P}_1\right)$ superelastic channel is shown in figure 2(*a*). Modulation curves for the elastic channel for laser-centre and laser-low arrangements are shown in figures 2(*b*) and (*c*), respectively. The various contributions to the measured scattering intensity are indicated. In order to extract collision parameters and magnetic sublevel-specific differential scattering cross sections from the intensity modulation curves, one must obtain these modulation curves with several laser geometries for each $E_0, \theta$ case. We obtained these curves using four laser geometries ($\theta_\nu = 45^\circ$ and $90^\circ$ both for scattering to the left- and to the right-hand side, corresponding to $\phi_n = 0^\circ$ and $180^\circ$). The procedure for achieving these measurements was as follows: after the laser beam and Ba beam conditions were stabilized, the impact energy and scattering angle calibrations were carried out. The impact energy scale was calibrated against the well established 19.366 eV resonance (Brunt *et al* 1977) in the elastic channel for He at $90^\circ$ scattering angle and the true

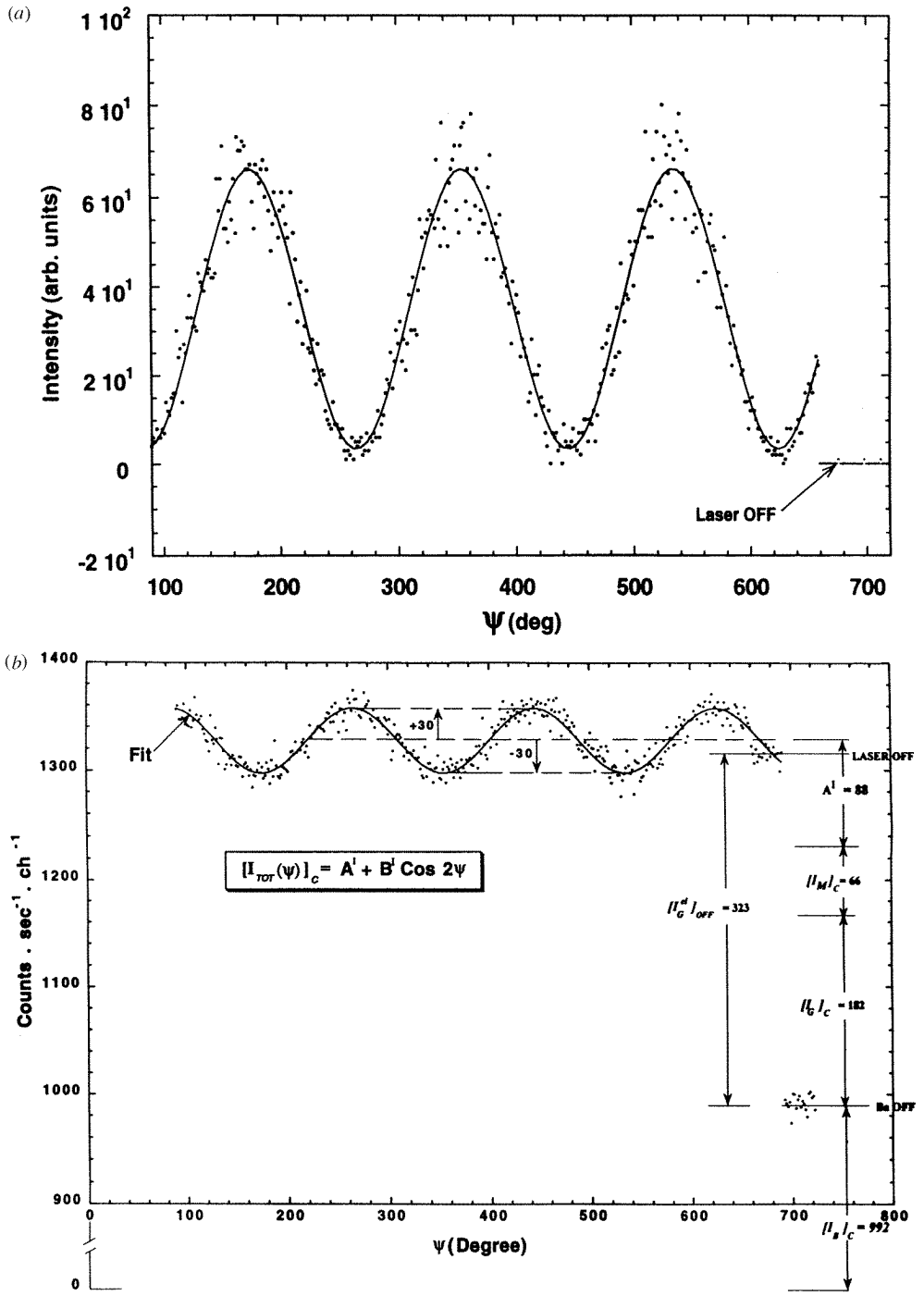


**Figure 2.** Scattering intensity modulation curves obtained at $E_0 = 20$ eV, $\theta = 20^\circ$ with $\theta_n = 135^\circ$, $\phi_n = 180^\circ$. (*a*) In the superelastic channel with laser-centre arrangement (the background is shown on the right-hand side). (*b*) In the elastic channel with laser-centre arrangement. (The various contributions to the total scattering intensity are indicated and the upper right-hand index, $I$ for $A$ and $B$ refers to the fact that they are associated with the intensity modulation curve.) (*c*) In the elastic channel with laser-low arrangement.

(*c*)

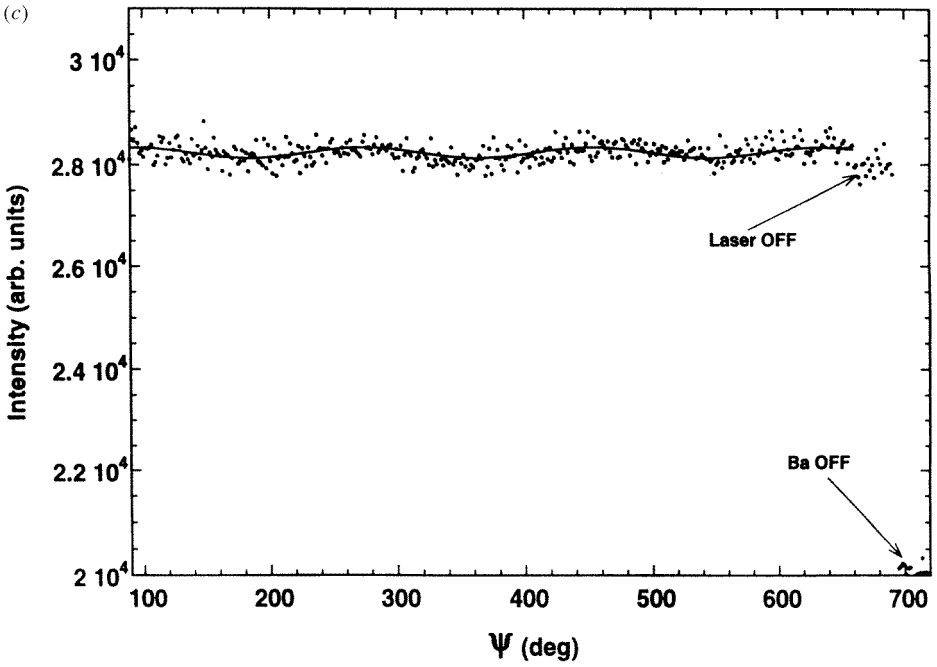


**Figure 2.** Continued.

zero scattering angle was determined from the symmetry of the $({}^1S_0{-}{}^1P_1)$ scattering intensity around the nominal zero angle. For fixed $E_0$, $\theta$ and laser geometry the measurements included the following steps:

(a) The scattering intensities were measured with the *laser-centre* arrangement in the $({}^1S_0{-}{}^1P_1)$ inelastic channel ($\psi$ can have any value) for the following cases: (i) laser on, Ba on, (ii) laser off, Ba on, (iii) laser off, Ba off. The scattering intensity in the $({}^1P_1{-}{}^1S_0)$ superelastic channel was also measured for laser on, Ba on and $\psi = \psi_{max}$ ($\psi_{max}$ is the polarization angle which yields the maximum superelastic signal). We refer to these measurements as check measurements.

(b) The elastic modulation curve was obtained with the *laser-centre* arrangement using repetitive, multichannel scaling scans. The full scan consisted of three sections. In the first section the elastic scattering signal as a function of $\psi$ was recorded from 90° to 690°. This was followed by a section representing the signal with the laser turned off and finally the section with both the laser and the Ba beams turned off.

(c) The elastic intensity modulation curve was determined with the *laser-low* arrangement the same way as in (b).

(d) The check measurements were carried out with the *laser-low* arrangement. (The same procedure as in (a) but no superelastic intensity measurements were needed.)

(e) The check measurements were carried out with the *laser-centre* arrangement. (The same procedure as in (a).)

(f) The superelastic intensity modulation curve was determined with the *laser-centre* arrangement following the same procedure as in (b).

(g) The check measurements were carried out with the *laser-centre* arrangement. (The same procedure as in (a).)

All of the above measurements were carried out for each of the four laser geometries, representing 116 measurements for each $E_0, \theta$ case. In addition, the fluorescence intensity from the laser-excited Ba atoms, the laser power and the barium oven temperature were continuously monitored, and the impact energy and zero-angle calibrations were repeated upon completion of the measurements.

This elaborate procedure was necessary to ensure nearly identical scattering and laser pumping conditions during the acquisition of all data for a fixed $E_0, \theta$ case and to supply all the data needed for the subtraction of the background, for separation of the elastic signal contributions and for the normalization of the intensities to the corresponding cross sections, as well as to permit the extraction of the desired parameters and cross sections. It should be noted that the elastic signal with the laser-low arrangement was constant within ∼1% as $\psi$ was rotated. Therefore, a single measurement, rather than the full modulation curve, would have been sufficient for this arrangement. However, we carried out the full modulation measurement for reasons of convenience and consistency and to check the presence (absence) of modulation in this signal.

### *2.3. Determination of the target beam composition*

As indicated above, the target Ba beam, depending on the experimental conditions, contained a number of different Ba species. The conversion of the measured elastic scattering signals to the corresponding cross sections requires knowledge of the relative populations of all species present in the electron–atom interaction region. All of these populations can be derived from a set of measurements as described in appendix A.

### *2.4. Magnetic sublevel superposition coefficients and populations for the $^1P_1$ atoms*

A linearly polarized laser beam excites the $^{138}$Ba atoms from the ground $^1S_0(M = 0)$ to the $^1P_1(M = 0)$ state with reference to the photon frame. A transformation of the excited state wavefunction to the electron collision frame (forward collision frame) results in a wavefunction which is, in general, a linear superposition of the three magnetic sublevel wavefunctions. It can be shown (Li and Zetner 1996, Zetner 1994) that for the case when the laser beam is in the scattering plane (in-plane laser geometry), the expansion coefficients are given as

$$C_0 \equiv C(M=0) = -\sin\theta_n \cos\psi \tag{1a}$$

$$C_1 \equiv C(M=1) = \pm\frac{1}{\sqrt{2}}\left[e^{i\psi}\sin^2\left(\tfrac{1}{2}\theta_n\right) - e^{-i\psi}\cos^2\left(\tfrac{1}{2}\theta_n\right)\right] \tag{1b}$$

$$C_{-1} \equiv C(M=-1) = \pm\frac{1}{\sqrt{2}}\left[e^{i\psi}\cos^2\left(\tfrac{1}{2}\theta_n\right) - e^{-i\psi}\sin^2\left(\tfrac{1}{2}\theta_n\right)\right]. \tag{1c}$$

The population fraction in the magnetic sublevel $M$ is given by $|C(M)|^2$ and $\sum_M |C(M)|^2 = 1$. The polar angles $\theta_n, \phi_n$ have been defined earlier, and in equations (10*b*) and (10*c*) the + and − signs refer to $\phi_n = 0^\circ$ and $180^\circ$, respectively.

Only alignment (no orientation) is created by the linearly polarized laser beam and thus we have

$$|C_0|^2 \equiv |C(M=0)|^2 = \sin^2\theta_n \cos^2\psi \tag{2a}$$

$$|C_1|^2 \equiv |C(M=1)|^2 = |C(M=-1)|^2$$
$$= \tfrac{1}{2}\left\{\cos^2\psi\left[\cos^4\left(\tfrac{1}{2}\theta_n\right) - 2\sin^2\left(\tfrac{1}{2}\theta_n\right)\cos^2\left(\tfrac{1}{2}\theta_n\right) + \sin^4\left(\tfrac{1}{2}\theta_n\right)\right] + \sin^2\psi\right\}. \tag{2b}$$

**Table 1.** Summary of magnetic sublevel superposition coefficients and populations of special importance to us here.

| $\theta_v$ (deg) | $\theta_n$ (deg) | $\phi_n$ (deg) | $\psi$ (deg) | $C_0$ | $C_1$ | $C_{-1}$ | $N_0$ | $N_1 = N_2$ |
|---|---|---|---|---|---|---|---|---|
| 45 | 135 | 0 | 0 | $-1/\sqrt{2}$ | $1/2$ | $-1/2$ | $1/2$ | $1/4$ |
| | | 180 | 0 | $-1/\sqrt{2}$ | $-1/2$ | $1/2$ | $1/2$ | $1/4$ |
| | | 0 | 90 | 0 | $\mathrm{i}/\sqrt{2}$ | $\mathrm{i}/\sqrt{2}$ | 0 | $1/2$ |
| | | 180 | 90 | 0 | $-\mathrm{i}/\sqrt{2}$ | $-\mathrm{i}/\sqrt{2}$ | 0 | $1/2$ |
| | | 0 | $\psi_m$ | $-1/\sqrt{3}$ | $1/\sqrt{6}(1+\mathrm{i})$ | $1/\sqrt{6}(\mathrm{i}-1)$ | $1/3$ | $1/3$ |
| | | 180 | $\psi_m$ | $-1/\sqrt{3}$ | $-1/\sqrt{6}(1+\mathrm{i})$ | $-1/\sqrt{6}(\mathrm{i}-1)$ | $1/3$ | $1/3$ |
| 90 | 90 | 0 | 0 | $-1$ | 0 | 0 | 1 | 0 |
| | | 180 | 0 | $-1$ | 0 | 0 | 1 | 0 |
| | | 0 | 90 | 0 | $\mathrm{i}/\sqrt{2}$ | $\mathrm{i}/\sqrt{2}$ | 0 | $1/2$ |
| | | 180 | 90 | 0 | $-\mathrm{i}/\sqrt{2}$ | $-\mathrm{i}/\sqrt{2}$ | 0 | $1/2$ |
| | | 0 | $\psi_m$ | $-\sqrt{2}/3$ | $\mathrm{i}/\sqrt{6}$ | $\mathrm{i}/\sqrt{6}$ | $2/3$ | $1/6$ |
| | | 180 | $\psi_m$ | $-\sqrt{2}/3$ | $-\mathrm{i}/\sqrt{6}$ | $-\mathrm{i}/\sqrt{6}$ | $2/3$ | $1/6$ |

The magnetic sublevel superposition coefficients and the population fractions, for cases which are important here, are given in table 1. It can be seen from the table that:

(a) for any in-plane laser geometry, when $\psi = 90^\circ$, only the $M = 1$ and $M = -1$ sublevels are populated;
(b) for $\theta_v = 90^\circ$, $\phi_n = 0^\circ$ or $180^\circ$ and $\psi = 0^\circ$, only the $M = 0$ sublevel is populated;
(c) for $\theta_v = 45^\circ$, $\phi_n = 0^\circ$ or $180^\circ$ and $\psi = \psi_m$, the three magnetic sublevels are all equally populated (isotropic coherent state).

### *2.5. Extraction of the elastic scattering intensity modulation associated with the $^{138}Ba(^1P_1)$ atoms*

The measured elastic scattering intensity contains components associated with all species present in the target beam under the given experimental conditions. One has to determine the magnitude of these individual contributions in order to obtain the scattering intensity associated with the $^{138}\mathrm{Ba}(^1\mathrm{P}_1)$ atoms, $\left[I^{\mathrm{el}}_{\mathrm{cP}}(\psi)\right]_{\mathrm{C}}$. The steps involved in this determination are described in appendix B. The procedure for normalizing $\left[I^{\mathrm{el}}_{\mathrm{cP}}(\psi)\right]_{\mathrm{C}}$ to the absolute scale to obtain $\mathrm{DCS}^{\mathrm{el}}_{\mathrm{cP}}(\psi)$ is given in appendix C.

## 3. Interpretation of the cross section modulation equation

The cross section modulation curves can be represented as

$$\begin{aligned}\mathrm{DCS}^{\mathrm{el}}_{\mathrm{cP}}(\psi) &= A^{\mathrm{el}}_{\mathrm{exp}} + B^{\mathrm{el}}_{\mathrm{exp}}\cos 2\psi = \tfrac{3}{4}\,\mathrm{DCS}^{\mathrm{el}}_{\mathrm{P}}\left\{A^{\mathrm{el}} + B^{\mathrm{el}}\cos 2\psi\right\} \\ &\equiv \tfrac{3}{4}\,\mathrm{DCS}\{A + B\cos 2\psi\} \qquad (3)\end{aligned}$$

(see Zetner *et al* 1990). The modulation coefficients $A^{\mathrm{el}}_{\mathrm{exp}}$ and $B^{\mathrm{el}}_{\mathrm{exp}}$ are obtained from the cross section modulation curves by a least-squares fitting procedure and converted to $A^{\mathrm{el}}$ ($A$) and $B^{\mathrm{el}}$ ($B$) using the $\mathrm{DCS}^{\mathrm{el}}_{\mathrm{P}}$ (DCS) value, which is also determined from the present measurement (see equation (A9) in appendix A). Henceforth we drop the upper right index 'el' from all parameters and cross sections since we are now dealing only with elastic scattering. $A$ and $B$ are functions of the laser geometry and the electron collision parameters. From the modulation equations, determined at four different laser geometries, we have four sets of $A$,

$B$ values for each $E_0, \theta$ case, from which we can extract three collision (or equivalently three electron-impact coherence) parameters. Due to this overdetermination, we have 16 different meaningful combinations of three equations to solve for the three parameters which can be extracted from the present measurements. We used the average of these 16 sets of parameters as our final result.

These parameters can also be extracted from the unnormalized intensity modulation curves, which avoids the error associated with normalization.

In this procedure, the ratio

$$R \equiv \frac{I_{\min}}{I_{\max}} = \frac{I_{\mathrm{cP}}(\psi = 0^\circ)}{I_{\mathrm{cP}}(\psi = 90^\circ)} = \frac{A + B}{A - B} \tag{4}$$

is obtained at three different laser geometries and the resulting equations are solved for three parameters. We found, however, that this method resulted in larger error limits than the procedure described first.

Equation (3) can be interpreted in terms of two different elastic scattering processes:

(a)

$$^{138}\mathrm{Ba}\left(^1\mathrm{P}_1, M_i = \text{isotr., incoh.}\right) + \mathrm{e}(E_0) \rightarrow {}^{138}\mathrm{Ba}\left(^1\mathrm{P}_1, M_f = 0, \pm 1; \text{coh., align.}\right) + \mathrm{e}(E_0). \tag{5}$$

Here the initial state is isotropic and incoherent while the final state produced by the indicated electron scattering process is, in general, aligned and partially coherent.

(b)

$$^{138}\mathrm{Ba}\left(^1\mathrm{P}_1, M_i = 0, \pm 1; \text{coh., align.}\right) + \mathrm{e}(E_0) \rightarrow {}^{138}\mathrm{Ba}\left(^1\mathrm{P}_1, M_f = \text{undet.}\right) + \mathrm{e}(E_0). \tag{6}$$

Here the initial state is produced by laser excitation (coherent and generally aligned), while there is no information on the coherence or polarization properties of the final state.

*The first interpretation scheme* is based on the theory of Macek and Hertel (1974) in terms of equation (5) which is a hypothetical process commonly called the 'inverse' process. It is 'inverse' with respect to the actual experimentally measured scattering process given by equation (6). However, these two processes are not strictly time-inverse processes even for the $\left(^1\mathrm{P}_1{-}^1\mathrm{P}_1\right)$ elastic scattering since the laser-produced and the electron-impact-produced states are not, in general, the same. In this scheme the cross section modulation equations are evaluated with

$$A = 1 + \cos^2\theta_n + \lambda\left(1 - 3\cos^2\theta_n\right) + (\lambda - 1)\cos\varepsilon\left(1 - \cos^2\theta_n\right) + k\sin 2\theta_n \cos\phi_n \tag{7a}$$

$$B = (3\lambda - 1)\sin^2\theta_n + (1 - \lambda)\cos\varepsilon\left(1 + \cos^2\theta_n\right) + k\sin 2\theta_n \cos\phi_n \tag{7b}$$

where

$$k = 2\sqrt{\lambda(1 - \lambda)}\,\cos\Delta\cos\tilde{\chi} \tag{7c}$$

(see Zetner *et al* 1990).

For the present experiments we have, for scattering to the *left* (with respect to the $Z_{\mathrm{lab}}$): for

$$0^\circ \leqslant \theta \leqslant 180^\circ - \theta_v \qquad \theta_n = \theta_v + \theta \qquad \phi_n = \phi_v - 180^\circ = 0^\circ$$

and for

$$180^\circ - \theta_v \leqslant \theta \leqslant 180^\circ \qquad \theta_n = 360^\circ - \theta_v - \theta \qquad \phi_n = \phi_v = 180^\circ$$

and for scattering to the *right*: for

$$0^\circ \leqslant \theta \leqslant \theta_v \qquad \theta_n = \theta_v - \theta \qquad \phi_n = \phi_v = 180^\circ$$

and for

$$\theta_v \leqslant \theta \leqslant 180^\circ \qquad \theta_n = \theta - \theta_v \qquad \phi_n = \phi_v - 180^\circ = 0^\circ.$$

As we indicated in section 2.1, in our experiments the laser itself was always on the same side of $\vec{k}_i$ as $X_{\text{lab}}$, and, therefore, $\phi_v$ was always 180°. Scattering to the left (right) here means that $\vec{k}_f$ is on the same (opposite) side of $\vec{k}_i$ as $X_{\text{lab}}$. In equation (7) the dependence of $A$ and $B$ on the laser geometry and on the EICPs ($\lambda$, $\cos\varepsilon$, $\cos\Delta$ and $\cos\tilde{\chi}$) are shown explicitly and the definitions of $\theta_n$ and $\phi_n$ assure that the EICPs (and the magnetic sublevel cross sections derived from them) are referred to the collision frame associated with the inverse elastic scattering process. That is, the reference direction is taken along the momentum vector of the incoming electron for this inverse process. Dropping the P index (which refers to the initial 6s6p $^1P_1$ level), the EICPs are defined (da Paixao *et al* 1980) as

$$\lambda = \frac{\text{DCS}(M_f = 0)}{\text{DCS}} \tag{8a}$$

$$\cos\varepsilon = -\frac{\frac{1}{3}\sum_{M_i} f(M_i, M_f = 1) f^*(M_i, M_f = -1)}{\text{DCS}(M_f = 1)} \tag{8b}$$

$$\cos\Delta = \frac{\frac{1}{3}\left|\sum_{M_i} f(M_i, M_f = 1) f^*(M_i, M_f = 0)\right|}{\sqrt{\text{DCS}(M_f = 1)\,\text{DCS}(M_f = 0)}} \tag{8c}$$

and

$$\cos\tilde{\chi} = \cos\left\{\arg\left[\frac{1}{3}\sum_{M_i} f(M_i, M_f = 1) f^*(M_i, M_f = 0)\right]\right\}. \tag{8d}$$

Here $f$ and DCS represent the scattering amplitude and differential scattering cross section, respectively, and the initial and final magnetic sublevel quantum numbers ($M_i$ and $M_f$) take the values of $-1$, 0 and 1. The convention we use here implies averaging over omitted initial and a summation over omitted final quantum number(s), for example,

$$\text{DCS}(M_f = 0) = \frac{1}{3}\sum_{M_i} \text{DCS}(M_i, M_f = 0) \tag{9a}$$

and

$$\text{DCS} = \frac{1}{3}\sum_{M_i}\sum_{M_f} \text{DCS}(M_i, M_f). \tag{9b}$$

The EICPs characterize the state prepared by the inverse electron collision process. They are equivalent to the density matrix of the state prepared in the inverse-electron scattering process. For example, $\cos\varepsilon$ corresponds to the off-diagonal matrix element representing the $M_i$-averaged interference between the $f(M_i, M_f = 1)$ and $f(M_i, M_f = -1)$ scattering amplitudes and $\tilde{\chi}$ is the $M_i$-averaged phase difference between the $f(M_i, M_f = 1)$ and $f(M_i, M_f = 0)$ scattering amplitudes. From the present experiments we can deduce only $\lambda$, $\cos\varepsilon$ and $k$. From $\lambda$ and DCS we obtain the DCS($M_f = 0$) value and in turn we have DCS($M_f = 1$) = DCS($M_f = -1$) = $\frac{1}{2}$[DCS − DCS($M_f = 0$)]. The present parameters could be transformed to the so-called 'natural frame' parameters if desired (see Andersen *et al* (1988) for the necessary equations).

*In the second evaluation scheme*, the cross section modulation equations are evaluated with

$$A = 1 + \cos^2\theta_n + p_1\left(1 - 3\cos^2\theta_n\right) + (p_1 - 1)\,p_2\left(1 - \cos^2\theta_n\right) + h\sin 2\theta_n\cos\phi_n \tag{10a}$$

$$B = (3p_1 - 1)\sin^2\theta_n + (1 - p_1)\,p_2\left(1 + \cos^2\theta_n\right) + h\sin 2\theta_n\cos\phi_n \tag{10b}$$

where

$$h = 2\sqrt{p_1(1-p_1)}\, p_3 p_4. \tag{10c}$$

For the present experiments, we have, for all values of $\theta$:

$$\theta_n = 180^\circ - \theta_v$$
$$\phi_n = \phi_v - 180^\circ = 0^\circ$$

for scattering to the left, and

$$\phi_n = \phi_v = 180^\circ$$

for scattering to the right. The collision parameters ($p_1$, $p_2$, $p_3$ and $p_4$) are defined similarly to the EICPs as

$$p_1 = \frac{\mathrm{DCS}(M_i = 0)}{3\,\mathrm{DCS}} \tag{11a}$$

$$p_2 = -\frac{\sum_{M_f} f(M_i = 1, M_f) f^*(M_i = -1, M_f)}{\mathrm{DCS}(M_i = 1)} \tag{11b}$$

$$p_3 = \frac{|\sum_{M_f} f(M_i = 1, M_f) f^*(M_i = 0, M_f)|}{\sqrt{\mathrm{DCS}(M_i = 1)\,\mathrm{DCS}(M_i = 0)}} \tag{11c}$$

and

$$p_4 = \cos\left\{\arg\left[\sum_{M_f} f(M_i = 1, M_f) f^*(M_i = 0, M_f)\right]\right\}. \tag{11d}$$

These do not yield information about the state prepared by the electron-impact excitation process, but are reflective of the coherence properties of the state produced by the laser excitation. In principle, these collision parameters are related to the EICPs. At the level of scattering amplitudes, the time-reversal symmetry would apply if both sets of amplitudes were given with respect to the same reference coordinate frame (see appendix D). The practical significance of the collision parameters is that, from them, we can generate cross sections for elastic scattering by atoms produced by any laser geometry and polarization, $[\mathrm{DCS}_{\mathrm{cP}}(\theta_n, \phi_n, \psi)]$ or equivalently by atoms in any coherent superposition state of the magnetic sublevels, $\mathrm{DCS}(M_i = 0, \pm 1; \mathrm{coh.}) \equiv \sum_{M_f} \left|\sum_{M_i} C_{M_i} f(M_i, M_f)\right|^2$. Here $C_{M_i}$ are the complex coefficients in the superposition which are given by equations (1*a*)–(1*c*).

Three of the $\mathrm{DCS}_{\mathrm{cP}}(\theta_n, \phi_n; \psi)$ values are easily obtained from the cross section modulation curves and are of particular importance.

(a) For any laser geometry and $\psi = 90^\circ$, the cross section is a maximum or minimum depending on whether $B$ is negative or positive and it corresponds to an initial state which is a coherent superposition of the $M_i = 1$ and $-1$ magnetic sublevels with equal coefficients. We have $[\mathrm{DCS}_{\mathrm{cP}}(\theta_n, \phi_n, 90^\circ)] = \sum_{M_f} |C_1 f(1, M_f) + C_{-1} f(-1, M_f)|^2 \equiv \mathrm{DCS}(M_i = \pm 1; \mathrm{coh.})$. The modulation equation yields

$$\mathrm{DCS}_{\mathrm{cP}}(\theta_n, \phi_n, 90^\circ) = \tfrac{3}{2}\,\mathrm{DCS}\{1 - p_1 - p_2 + p_1 p_2\}. \tag{12}$$

(b) For $\theta_n = \theta_v = 90^\circ$, $\phi_n = 0^\circ$ or $180^\circ$ and $\psi = 0^\circ$, we have

$$\mathrm{DCS}_{\mathrm{cP}}(90^\circ, 0^\circ, 0^\circ) = \mathrm{DCS}_{\mathrm{cP}}(90^\circ, 180^\circ, 0^\circ) = \sum_{M_f} |C_0 f(0, M_f)|^2 \equiv \mathrm{DCS}(M_i = 0) \tag{13}$$

and this is a minimum or maximum depending on whether $B$ is negative or positive, i.e. just the opposite to case (a). The modulation equation yields

$$\mathrm{DCS}_{\mathrm{cP}}(90^\circ, 0^\circ, 0^\circ) = \mathrm{DCS}_{\mathrm{cP}}(90^\circ, 180^\circ, 0^\circ) = \tfrac{3}{4}\,\mathrm{DCS}\{4\lambda\}. \tag{14}$$

(c) For $\theta_n = 135^\circ$ ($\theta_v = 45^\circ$) and $\psi = \psi_m$, we have

$$\mathrm{DCS_{cP}}(135^\circ, \phi_n, \psi_m) = \sum_{M_f} \left| \sum_{M_i} C_i(\phi_n) f(M_i, M_f) \right|^2$$
$$\equiv \mathrm{DCS}(M_i = 0, \pm 1; \text{coh.}) \tag{15}$$

with $|C_0|^2 = |C_1|^2 = |C_{-1}|^2$ for $\phi_n = 0^\circ$ or $180^\circ$.

The modulation equations for these cases yield

$$\mathrm{DCS_{cP}}(135^\circ, 0^\circ, \psi_m) = \mathrm{DCS}\{1 - h\} \tag{16a}$$

$$\mathrm{DCS_{cP}}(135^\circ, 180^\circ, \psi_m) = \mathrm{DCS}\{1 + h\}. \tag{16b}$$

The initial scattering state prepared by the laser excitation here is *isotropic and coherent*. The coherence introduces the azimuthal angle dependence into the scattering (left/right scattering asymmetry) and the two cross sections differ by $2h$. For an *isotropic incoherent* initial state, we have the azimuthal-angle-independent cross section, DCS. It is also obvious from equations (16*a*) and (16*b*) that $\mathrm{DCS_{cP}}(135^\circ, 0^\circ, \psi_m) + \mathrm{DCS_{cP}}(135^\circ, 180^\circ, \psi_m) = 2\,\mathrm{DCS}$. We utilized this relationship in our present work to determine the DCS values.

The azimuthal (left/right scattering) asymmetry parameter (As), in general, is given as

$$\mathrm{As}(\theta_n, \psi) = \frac{\mathrm{DCS_{cP}}(\theta_n, 0^\circ, \psi) - \mathrm{DCS_{cP}}(\theta_n, 180^\circ, \psi)}{\mathrm{DCS_{cP}}(\theta_n, 0^\circ, \psi) + \mathrm{DCS_{cP}}(\theta_n, 180^\circ, \psi)} \tag{17a}$$

$$= \frac{2\sqrt{p_1(1-p_1)}\, p_3 p_4 \sin 2\theta_n (1 + \cos 2\psi)}{1 + \cos^2\theta_n + p_1\left(1 - 3\cos^2\theta_n\right) + (p_1 - 1) p_2 \sin^2\theta_n + \alpha} \tag{17b}$$

where $\alpha = \left[(3p_1 - 1)\sin^2\theta_n + (1 - p_1)p_2\left(1 + \cos^2\theta_n\right)\right]\cos 2\psi$.

## 4. Theoretical methods

We used a convergent close-coupling method to model the scattering process theoretically. The details of the application of this method to the calculation of electron scattering by alkaline-earth atoms have been given by Fursa and Bray (1997, 1998, 1999). Here we give only a short summary. The calculation of electron scattering and the target wavefunction is performed in the non-relativistic, $LS$-coupling framework. The barium atom is modelled as a quasi-two-electron atom, with two active electrons moving in the field of an inert Hartree–Fock core. Phenomenological one- and two-electron polarization potentials have been added to account for core polarization. The Ba atom wavefunctions were obtained from configuration-interaction expansions. The one-electron basis, used in the CI expansion, was obtained by diagonalizing the $Ba^+$ ion Hamiltonian in a large Laguerre basis. The parameters of the one-electron polarization potential were adjusted to obtain good agreement with the energy spectrum of the $Ba^+$ ion. The size of the Laguerre basis was increased until convergence in the description of the Ba discrete states (at least three for each target symmetry, if any) was achieved. The detailed description of the Ba wavefunctions which we used in the CCC calculations will be given elsewhere (Fursa and Bray 1999). Here we merely indicate that the calculated ionization energies of the ground and $(6s6p)^1P^o$ states were 5.237 and 2.973 eV, respectively. The calculated value of $\left(6s^2\right)^1S$–$(6s6p)^1P^o$ oscillator strength was $f = 1.69$ au. The agreement with the experimental values for ionization energies (5.211 and 2.972 eV, Moore 1949) and for the $f$-value ($f = 1.64$ au, Niggli and Huber 1989, Bizzarri and Huber 1990) is very good.

We included, in the close-coupling calculations, all negative energy states (relative to the $Ba^+$ ground state) obtained from diagonalization of the $Ba^+$ Hamiltonian in the CI basis. To account for coupling to the ionization continuum, we also included a large number of positive energy states. The total number of states was 115, consisting of 14 $^1$S, 17 $^1$P$_0$, 19 $^1$F$^o$, seven $^3$S, nine $^3$P$^o$, nine $^3$D$^o$, nine $^3$F$^o$ and two each of $^{1,3}$P$^o$, $^{1,3}$D$^o$, $^{1,3}$F$^o$ states. The large asymmetry in the number of singlet and triplet states is due to our interest in the scattering from a $^1$P state, for which, ionization into a singlet channel is substantially larger than ionization into the triplet channels at intermediate and high impact energies.

## 5. Results and discussions

Measurements were carried out at 20 eV impact energy and scattering angles of 10°, 15° and 20°, as described in section 2. From the experimental $A$ and $B$ values (which are listed in table 2) at each $E_0, \theta$, three electron-impact coherence parameters ($\lambda$, $\cos\varepsilon$ and $k$), three collision parameters ($p_1$, $p_2$ and $h$) and the magnetic sublevel averaged differential scattering cross section (DCS) were extracted, as discussed in section 3. From the $\lambda$, $p_1$ and DCS values, we obtained differential elastic scattering cross sections which are specific either in the final or the initial magnetic sublevel quantum number (and averaged over or summed over the other one). We also obtained the differential elastic scattering cross section directly from the modulation equations for a few specific cases, i.e. equations (12)–(16), corresponding to atomic ensembles in specific coherent magnetic sublevel superposition states generated by laser excitation with specific laser geometries and polarizations. These results are summarized in table 3, together with the corresponding theoretical values.

**Table 2.** Comparison of the experimental and calculated $A$ and $B$ coefficients and modulation depths ($B/A$) at $E_0 = 20.0$ eV (see equation (19)).

| $\theta$ | $\theta_n$ | $\phi_n$ | $A$ | | $B$ | | Modulation (%) | |
|---|---|---|---|---|---|---|---|---|
| (deg) | (deg) | (deg) | Experiment | Calculated | Experiment | Calculated | Experiment | Calculated |
| 10 | 135 | 0 | $1.30 \pm 0.39$ | 1.441 | $-0.15 \pm 0.05$ | −0.268 | $11.5 \pm 4.9$ | 18.6 |
| | 135 | 180 | $1.48 \pm 0.44$ | 1.413 | $-0.21 \pm 0.06$ | −0.296 | $14.2 \pm 6.0$ | 21.0 |
| | 90 | 0 or 180 | $1.32 \pm 0.40$ | 1.414 | $-0.17 \pm 0.05$ | −0.296 | $12.6 \pm 5.3$ | 20.9 |
| 15 | 135 | 0 | $1.42 \pm 0.43$ | 1.564 | $-0.34 \pm 0.10$ | −0.427 | $23.8 \pm 10.1$ | 27.3 |
| | 135 | 180 | $1.50 \pm 0.45$ | 1.432 | $-0.44 \pm 0.13$ | −0.560 | $29.2 \pm 12.4$ | 39.1 |
| | 90 | 0 or 180 | $1.53 \pm 0.46$ | 1.559 | $-0.40 \pm 0.12$ | −0.432 | $26.2 \pm 11.1$ | 27.7 |
| 20 | 135 | 0 | $1.33 \pm 0.40$ | 1.665 | $-0.44 \pm 0.13$ | −0.581 | $32.9 \pm 14.0$ | 34.9 |
| | 135 | 180 | $1.69 \pm 0.51$ | 1.458 | $-0.61 \pm 0.18$ | −0.788 | $36.1 \pm 15.3$ | 54.1 |
| | 90 | 0 or 180 | $1.76 \pm 0.53$ | 1.680 | $-0.45 \pm 0.14$ | −0.566 | $25.4 \pm 10.1$ | 33.7 |

In our error estimation, we considered errors due to the measurement of the scattering intensities, to the separation of the various contributions to the measured elastic scattering signals, and to normalization. In addition the nonlinear propagation of the experimental errors into $\cos\varepsilon$, $k$, $p_2$ and $h$ was also considered. Estimated values for these latter error contributions were made on the basis of model calculations. In these we artificially introduced errors into the $A$ and $B$ coefficients (occurring in the set of three modulation equations used for extracting these parameters) and observed the consequent effect upon the extracted parameters.

CCC calculations were carried out at $E_0 = 20.0$ eV with scattering angles ranging from 0° to 180° in 1° steps. The results of these calculations were the complex scattering amplitudes $f(M_i, M_f)$ for elastic scattering by Ba$\left(\ldots 6s6p\ ^1P_1\right)$ atoms. From the scattering amplitudes,

**Table 3.** Comparison of present experimental and calculated cross sections and parameters at $E_0 = 20.0$ eV. The cross sections are in $10^{-16}$ cm$^2$ sr$^{-1}$ units.

| | $\theta = 10^\circ$ | | $15^\circ$ | | $20^\circ$ | |
|---|---|---|---|---|---|---|
| | Experiment | Theory | Experiment | Theory | Experiment | Theory |
| $^{138}$Ba($6s6p\ ^1P_1$) state | | | | | | |
| $\lambda$ | $0.28 \pm 0.08$ | 0.28 | $0.27 \pm 0.08$ | 0.29 | $0.27 \pm 0.08$ | 0.30 |
| $\cos\varepsilon$ | $-0.10 \pm 0.05$ | $-0.19$ | $-0.29 \pm 0.15$ | $-0.41$ | $0.46 \pm 0.2$ | $-0.60$ |
| $k$ | $-0.052 \pm 0.160$ | 0.018 | $-0.036 \pm 0.10$ | 0.027 | $-0.213 \pm 0.350$ | 0.003 |
| $p_1$ | $0.29 \pm 0.09$ | 0.28 | $0.29 \pm 0.09$ | 0.28 | $0.33 \pm 0.10$ | 0.28 |
| $p_2$ | $-0.11 \pm 0.06$ | $-0.19$ | $-0.32 \pm 0.16$ | $-0.39$ | $-0.56 \pm 0.28$ | $-0.56$ |
| $h$ | $-0.067 \pm 0.150$ | $-0.014$ | $-0.024 \pm 0.10$ | $-0.066$ | $-0.135 \pm 0.200$ | $-0.104$ |
| DCS | $88.2 \pm 26.5$ | 78.3 | $16.3 \pm 4.9$ | 21.7 | $6.7 \pm 2.0$ | 7.2 |
| $\mathrm{DCS}(M_f = 1)$ $= \mathrm{DCS}(M_f = -1)$ | $31.9 \pm 9.6$ | 28.1 | $6.0 \pm 1.8$ | 7.7 | $2.5 \pm 0.8$ | 2.5 |
| $\mathrm{DCS}(M_f = 0)$ | $24.5 \pm 7.4$ | 22.1 | $4.4 \pm 1.3$ | 6.4 | $1.8 \pm 0.5$ | 2.2 |
| $\mathrm{DCS}(M_i = 1)$ $= \mathrm{DCS}(M_i = -1)$ | $94.1 \pm 28.2$ | 84.7 | $17.6 \pm 5.3$ | 23.4 | $6.8 \pm 2.0$ | 7.8 |
| $\mathrm{DCS}(M_i = 0)$ | $76.4 \pm 22.9$ | 65.7 | $13.8 \pm 4.1$ | 18.3 | $6.6 \pm 2.0$ | 6.0 |
| $\mathrm{DCS}(M_i = \pm 1$ coh.) | $102.2 \pm 30.7$ | 100.4 | $23.0 \pm 6.9$ | 32.4 | $10.5 \pm 3.2$ | 12.2 |
| Metastable ($^1D_2$ and $^3D_2$ states) | | | | | | |
| $\mathrm{DCS}_m$ | $57.8 \pm 17.3$ | 47.6 | $17.9 \pm 5.4$ | 17.7 | $7.1 \pm 2.1$ | 8.1 |
| Ground $^1S_0$ state | | | | | | |
| $\mathrm{DCS}_{\mathrm{gnd}}$ | $69.6 \pm 17.4$[a] | 63.3[c] | $15.5 \pm 3.9$[a] | 20.1[c] | $5.62 \pm 1.4$[a] | 7.34[c] |
| | $69.3 \pm 13.9$[b] | | $16.9 \pm 3.4$[b] | | $6.18 \pm 1.24$[b] | |

[a] Wang *et al* (1994).
[b] Present results.
[c] Fursa and Bray (1998).

we calculated the EICPs ($\lambda$, $\cos\varepsilon$, $\cos\Delta$, $\cos\tilde{\chi}$ and $k$), the collision parameters ($p_1$, $p_2$, $p_3$, $p_4$ and $h$) and the various elastic differential scattering cross sections ($\mathrm{DCS}(M_i, M_f)$, $\mathrm{DCS}(M_f)$, $\mathrm{DCS}(M_i)$, $\mathrm{DCS}(M_i = \pm 1$ coh.)). We also explicitly calculated the values of $\mathrm{DCS}_{\mathrm{cP}}(\theta_n, \phi_n, \psi)$ and $\mathrm{As}(\theta_n, \psi)$ for $\theta_n = 135^\circ$, $\phi_n = 0^\circ$ and $180^\circ$ and $\psi = 0^\circ$ and $\psi_m$ as well as the $A(\theta_n, \phi_n)$ and $B(\theta_n, \phi_n)$ values for $\theta_n = 135^\circ$ and $90^\circ$ and $\phi_n = 0^\circ$ and $180^\circ$. From the various differential cross sections, we calculated the corresponding integral cross sections and then obtained the alignment creation cross sections. In the following discussion, we present some of these results and compare experimental and theoretical results.

The dimensionless modulation parameter, $B(\theta_n, \phi_n)$ determines the magnitude of the modulation, which is zero when $B = 0$, as well as the phase of the modulation with $\psi$. Note that $\mathrm{DCS}(\psi = 90^\circ)$ is maximum (minimum) when $B$ is negative (positive). We found that $B$ assumes extreme values at scattering angles where the cross sections have deep minima. The value of $B$ is strongly angle dependent and changes sign at several angles (for a fixed $E_0$), causing the modulation to disappear at these angles. At $\theta = 0^\circ$ (and $180^\circ$), $B(\theta_n, 0^\circ) = B(\theta_n, 180^\circ)$ and $A(\theta_n, 0^\circ) = A(\theta_n, 180^\circ)$, since there is no azimuthal symmetry. A comparison of the experimental and calculated $A$ and $B$ coefficients is given in table 2.

Figure 3 shows the electron-impact coherence parameters $\lambda$, $\cos\varepsilon$ and $k$. The parameter $\lambda$ shows little change with the scattering angle, indicating that the angular dependence of $\mathrm{DCS}(M_f)$ and DCS involved are very similar. This behaviour is quite different from that encountered when averaging in $M_i$, for $\mathrm{DCS}(M_f)$ is absent; that is, when the initial state is non-degenerate (e.g. $\lambda$ parameters for electron-impact excitation of $^1S_0$ atoms). The experimental

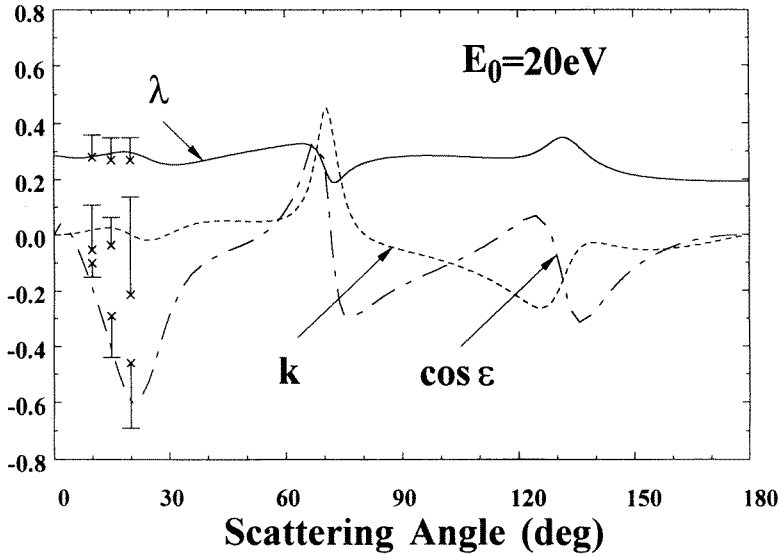


**Figure 3.** The angular dependence of the EICPs $(\lambda, \cos\varepsilon, k)$ for $E_0 = 20$ eV. The curve corresponds to the calculated values. The experimental results are indicated by crosses and the error limits are shown. (The $Y$-scale is enlarged to show details and only half of the experimental error limits are indicated to avoid overlap and confusion.)

$\lambda$ values are in excellent agreement with the calculated ones. The $\cos\varepsilon$ parameter, representing the normalized interference between the $f(M_f = 1)$ and $f(M_f = -1)$ amplitudes, varies widely with $\theta$ and changes sign several times over the full angular range. Extreme values occur at angles where the DCS$(M_f)$ values exhibit deep minima (see below), but also appear at other angles. Agreement between experiment and theory for $\cos\varepsilon$ is almost within the error bars. The somewhat larger deviations than in the case of $\lambda$ might be due to larger experimental uncertainties or possibly to spin–orbit coupling which was neglected in the calculations. The $\lambda$ and $\cos\varepsilon$ parameters, in effect, represent the two alignment parameters $A_0 = \frac{1}{2}(1 - 3\lambda)$ and $A_{2+} = \frac{1}{2}(\lambda - 1)\cos\varepsilon$ (see, e.g., Andersen *et al* 1988). The $k$ parameter is a complicated function of $\lambda$, $\cos\Delta$ and $\cos\tilde{\chi}$. The calculated values are small and show some variation with $\theta$. The experimental values are also small and in that respect are in good agreement with the theory, but they are associated with large error limits. The calculated values of $\cos\Delta$ and $\cos\tilde{\chi}$ are shown in figure 4. Both of these parameters vary rapidly with the scattering angle. It should be noted that the deviation of the calculated $\cos\varepsilon$ and $\cos\Delta$ values from unity is not an indication of the presence of spin–orbit coupling but is strictly due to averaging over $M_i$ in as much as the spin–orbit coupling effect was neglected in the calculation.

The collision parameters $p_1$, $p_2$ and $h$ are shown in figure 5. To $p_1$ the same comments apply as for $\lambda$ above. The angular dependence of $p_2$ is similar to that of $\cos\varepsilon$. Again the agreement between experiment and theory is excellent for $p_1$ and good for $p_2$. The same general comments apply to the $h$ parameter as to $k$. The calculated $h$ and $k$ values exhibit a very similar angular dependence. The calculated $p_3$ and $p_4$ (not shown) exhibit similar behaviour, with respect to $\theta$ as $\cos\Delta$ and $\cos\tilde{\chi}$, respectively, but there are significant differences in magnitude at certain angles.

The parameters $\cos\varepsilon$, $\cos\Delta$, $k$, $p_2$, $p_3$ and $h$ are zero for scattering angles equal to $0^\circ$ and $180^\circ$ (for any $E_0$). This is due to the fact that the values of $f(M_i, M_f)$ are zero at $\theta = 0^\circ$

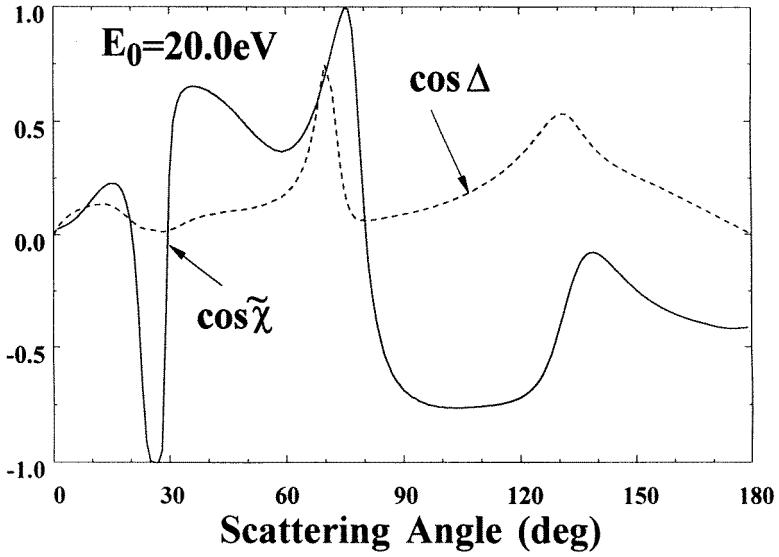


**Figure 4.** The calculated EICPs cos Δ and cos $\tilde{\chi}$ at $E_0 = 20.0$ eV.

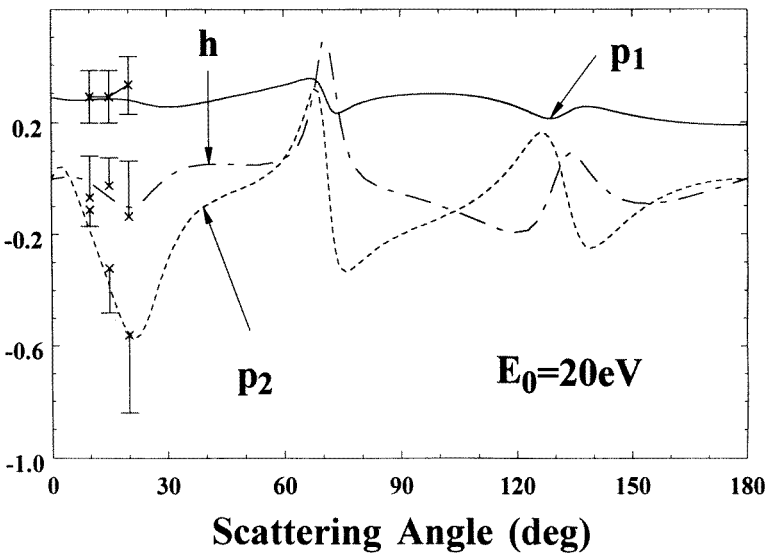


**Figure 5.** The angular dependence of the collision parameters ($p_1$, $p_2$ and $h$). The symbols and energy are the same as for figure 3.

and 180° for $M_i \neq M_f$ and in the bilinear combinations occurring in equations (8*b*), (8*c*), (11*a*) and (11*c*), one of the components will always be zero. The values of cos $\tilde{\chi}$ and $p_4$ are undetermined at $\theta = 0°$ and 180° for the same reason, since they represent the argument of a complex number which is zero. At $\theta = 0°$ and 180°, the distinction between forward and inverse processes disappears, the EICPs and collision parameters become the same and DCS($M_i$) = DCS($M_f$). Cos $\varepsilon$ ($p_2$) also becomes zero at certain intermediate scattering angles (for a given $E_0$), when the real number defined by the numerator of equation (8*b*)

(equation (11*b*)) becomes zero. Although cos Δ ($p_3$) could also become zero at intermediate scattering angles when the numerator of equation (8*c*) (equation (11*c*)) becomes zero, we have not encountered such a situation. Cos $\tilde{\chi}$ (and $p_4$) become zero at intermediate angles when the square brackets in the numerator of equation (8*d*) (equation (11*d*)) is a pure imaginary number and they become equal to one when these brackets yield a real number (+1 for $\tilde{\chi} = 0^\circ$ and $-1$ for $\tilde{\chi} = 180^\circ$). Such a case materializes for both cos $\tilde{\chi}$ and $p_4$, e.g. for cos $\tilde{\chi}$ at $E_0 = 20.0$ eV, $\theta = 26^\circ$ (figure 4). For cos $\varepsilon$, cos Δ, $p_2$ and $p_3$, values which approach ±1 have not been encountered. cos Δ (and $p_3$) is always positive since both the numerator and denominator in equation (8*c*) (and (11*c*)) are always positive. $k$ ($h$) is zero when cos Δ or cos $\tilde{\chi}$ is zero or $\lambda = 1$ ($p_3$ or $p_4$ is zero or $p_1 = 1$) and this occurs at several scattering angles.

The elastic differential scattering cross sections, which are specific in both the initial and final magnetic sublevel's quantum numbers, cannot be obtained from the present experiments. Representative examples of the calculated values (at $E_0 = 20$ eV) are given in figures 6(*a*)–(*c*). The cross section values depend strongly on the magnetic sublevel quantum numbers. For transitions where $\Delta M = 0$, the cross sections are large (about $100 \times 10^{-16}$ cm$^2$ sr$^{-1}$ at around 10°). The cross section curves are strongly forward-peaked and exhibit steep minima near 72° and 135°. For transitions where $\Delta M = \pm 1$, the cross sections are small (about $1 \times 10^{-16}$ cm$^2$ sr$^{-1}$ at around 10°), and approach zero at 0° and 180°, the minima are no longer sharp and are not localized near 72° and 135°. The DCS(1, −1) = DCS(−1, 1) curve ($\Delta M = \pm 2$) represents intermediate values ($10 \times 10^{-16}$ cm$^2$ sr$^{-1}$ near 10°) and angular behaviour. Figure 7 shows the DCS($M_f = 1$) and DCS($M_f = 0$) curves. The two curves are very similar, both in magnitude and in shape, with distinct minima at around 72° and 135°. This is due to the fact that in the averaging over $M_i$, the dominant terms (DCS(1, 1) and DCS(0, 0)) are very similar. The fully averaged cross section is also shown for comparison and again exhibits the characteristic behaviour associated with the $\Delta M = 0$ type scattering because this is the dominant contribution in the overall summation. The experimental cross sections are in excellent agreement with the theoretical results. Figure 8(*a*) shows the DCS($M_i = 0$), DCS($M_i = 1$) and DCS curves. These cross sections are very similar to those discussed above for specific $M_f$, and the same general remarks apply. Again the experimental results are in excellent agreement with the theory. The experimental DCS($M_i = 0$) values can be obtained from the $p_1$ and DCS values and also directly from the modulation curves. The value of this curve obtained for $\theta_n = 90^\circ$, $\phi_n = 0^\circ$ (or 180°) and $\psi = 0^\circ$ corresponds to DCS($M_i = 0$). For $E_0 = 20$ eV and at scattering angles of 10°, 15° and 20°, the modulation coefficient $B$ is negative and, therefore, this cross section corresponds to a minimum in the modulation curve. Figure 8(*b*) presents the cross sections corresponding to scattering by $^{138}$Ba atoms in a state which is a coherent superposition of the $M_i = 1$ and $-1$ magnetic sublevels with equal coefficients. These are compared with the DCS curve for $E_0 = 20$ eV. The DCS($M_i = \pm 1$; coh.) values (at any angle for a fixed $E_0$) can be read directly from the modulation curves obtained with $\psi = 90^\circ$ for any $\theta_n$ and $\phi_n$. At 20 eV and 10°, 15° and 20°, these points represent maxima since the $B$-values are negative. $B$ is sometimes positive at other impact energies and scattering angles, and for these cases the modulation curves are shifted by 180°. At $\theta = 0^\circ$ and 180°, we have DCS(1, 1) = DCS($M_i = \pm 1$ coh.) = DCS($M_i = 1$). This is again a consequence of the fact that $f(M_i, M_f) = 0$ for $M_i \neq M_f$ at $\theta = 0^\circ$ and 180°, and of the definition of these cross sections.

The azimuthal (left/right) scattering asymmetry parameter is, in general, defined by equation (17). The largest values for this parameter were found for atoms prepared with the laser-excitation conditions $\theta_n = 135^\circ$ and $\psi = 0^\circ$, and they can be given as As(135°, 0°) = $-2h/(1 + p_1 + p_2 - p_1 p_2)$. This parameter as a function of the scattering angle is shown in figure 9. It exhibits a strong dependence upon the scattering angle. Extreme values seem to

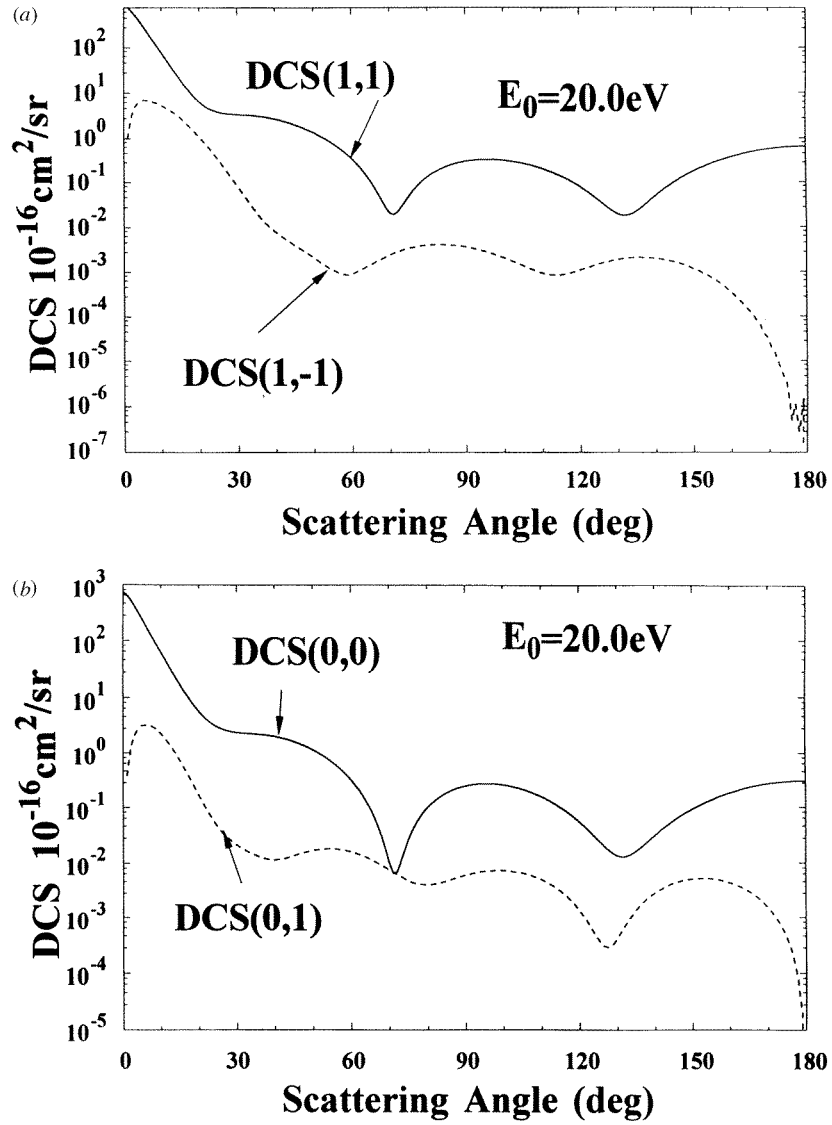


**Figure 6.** Calculated DCS($M_i$, $M_f$) angular dependence curves at $E_0 = 20$ eV. (*a*) DCS(1, 1) = DCS(−1, −1) and DCS(1, −1) = DCS(−1, 1); (*b*) DCS(0, 0) and DCS(0, 1) = DCS(0, −1) and (*c*) DCS(1, 0) = DCS(−1, 0).

be present at angles where the DCS($M_i = 1$) and DCS($M_i = 0$) cross section curves also have extrema. The asymmetry parameters associated with the laser excitation conditions of $\theta_n = 135^\circ$ and $\psi = \psi_m$ are given as As($135^\circ$, $\psi_m$) $= -h$, and can be visualized from the $h$ curves (e.g. figure 5). It is interesting to note that the non-zero value of As($135^\circ$, $\psi_m$) is the consequence of the coherences which are associated with the *coherent isotropic* initial scattering states prepared with laser excitation conditions $\theta_n = 135^\circ$, $\phi_n = 0^\circ$, $\psi = \psi_m$ and $\theta_n = 135^\circ$, $\phi_n = 180^\circ$, $\psi = \psi_m$. For an *incoherent isotropic* initial state, the cross sections for scattering to the left and right are equal and are given by the value of DCS. Therefore, no azimuthal asymmetry exists. The asymmetry parameters become zero due to

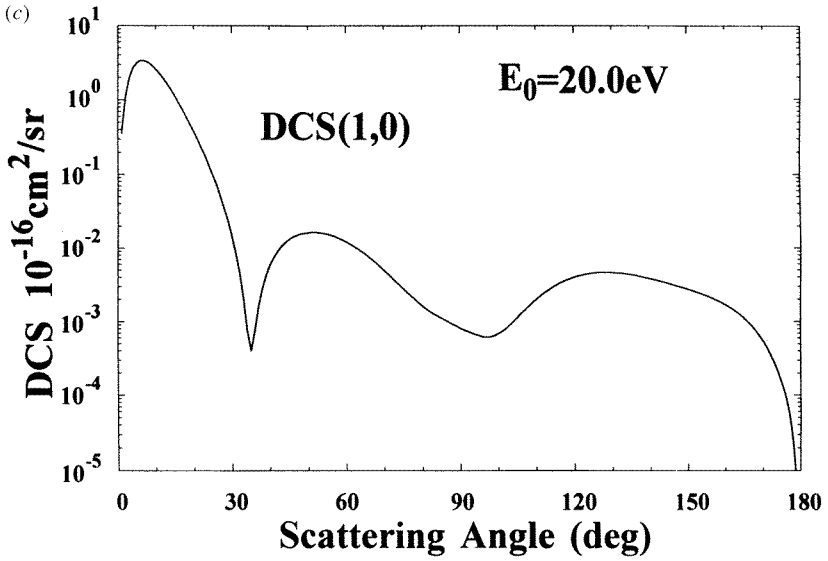


**Figure 6.** Continued.

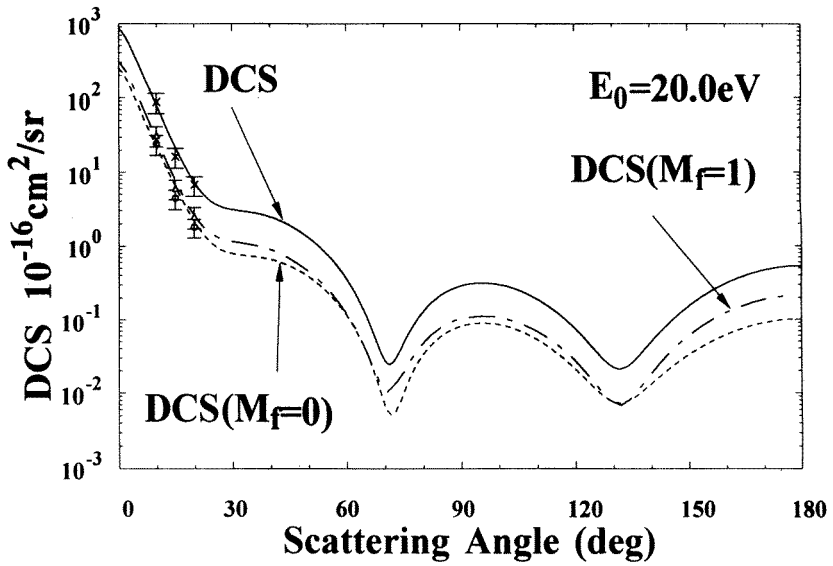


**Figure 7.** The angular dependence of DCS($M_f = 0$); DCS($M_f = 1$) = DCS($M_f = -1$) and DCS at $E_0 = 20$ eV. The corresponding experimental results are indicated by the symbols ○, △ and ×, respectively.

the nature of the target state generated by the laser excitation when $\psi = 90^\circ$ (for any $\theta_n$) and/or when $\theta_n = 0^\circ, 90^\circ$ or $180^\circ$ (for any value of $\psi$). It is easy to see from the scattering symmetry that the target atom charge distribution in these cases is such that there is no difference between scattering to the left or right. The asymmetry parameters can also become zero due to the particular nature of the scattering processes involved in the summation over $M_f$ for our measurements. This could be due to $p_1$ and/or $p_3$ and/or $p_4$ being zero or to $p_1 = 1$. The

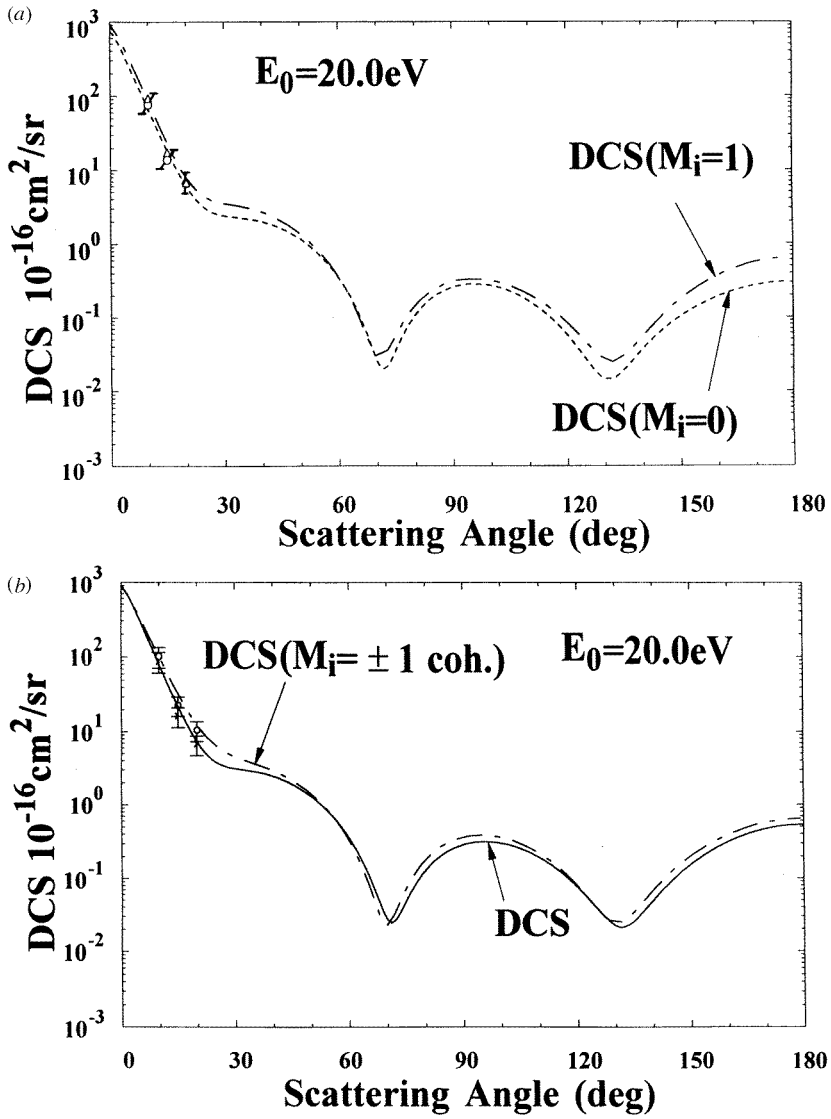


**Figure 8.** The angular dependence of differential scattering cross sections at $E_0 = 20$ eV. (*a*) DCS($M_i = 0$) and DCS($M_i = 1$) = DCS($M_i = -1$). The corresponding experimental results are indicated by the symbols ○ and △, respectively. (*b*) DCS($M_i = \pm 1$ coh.) and DCS. The corresponding experimental results are indicated by the symbols ○ and ×, respectively.

asymmetry parameter is zero at $\theta = 0^\circ$ or $180^\circ$ by necessity (for any $E_0$, $\theta_n$, $\psi$ value) as can be seen, for example, in figure 9. This is caused in equation (17*b*) by $p_3$ becoming zero at $\theta = 0^\circ$ and $180^\circ$, as mentioned above. The asymmetry parameter can also become zero at intermediate angles under certain conditions (see, e.g., figure 9). The CCC calculations show that, at these angles, $p_4$ becomes zero. A comparison of the asymmetry parameters corresponding to the two special cases discussed above is shown in figure 9.

Considering the complexity of the experiments and the fact that the theoretical calculations neglect spin–orbit-coupling effects, the general agreement between theory and experiment is

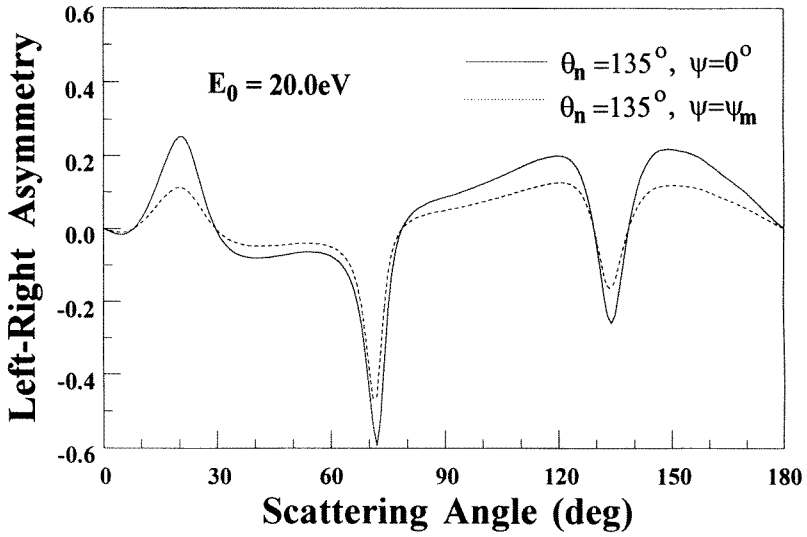


**Figure 9.** Comparison of the asymmetry parameters for laser conditions ($\theta_n = 135^\circ$, $\psi = 0^\circ$) and ($\theta_n = 135^\circ$, $\psi = \psi_m$) at $E_0 = 20$ eV.

surprisingly good for the $E_0 = 20$ eV, $\theta = 10^\circ, 15^\circ, 20^\circ$ cases. This agreement indicates that extended scattering volume effects (see Zetner *et al* 1990) are not important in the present measurements and that the CCC calculational scheme used here is applicable to elastic scattering by $\mathrm{Ba}(^1\mathrm{P}_1)$ atoms. The rate of convergence and the importance of the ionization channels in our calculations were investigated by also performing calculations with 55 discrete states in the expansion. The results of these calculations were found to be very similar to those described here, which included 115 states and accounted for coupling to the target ionization continuum. The reason for this agreement is that the dipole polarizability for the $\mathrm{Ba}(6s6p\ ^1\mathrm{P}_1)$ state is dominated by the discrete spectrum. The neglect of spin–orbit coupling in our calculations is justified by the good agreement between experiment and theory. The major effect of spin–orbit coupling in our case manifests itself in singlet–triplet mixing for the target atom. It is well known, however, that the mixing coefficient for the $^3\mathrm{P}_1$ $LS$ term is small (see, e.g., Bauschlicher *et al* 1985).

The good agreement between experiment and theory gives some assurance that the CCC method can be used reliably at other scattering angles and impact energies for obtaining the various integral elastic scattering and the alignment creation $Q_{CR}^{[2]} = \sqrt{\frac{2}{3}}[Q(M_f = 1) - Q(M_f = 0)]$ cross sections. Some of these cross sections are listed in table 4, which also shows a comparison between experimental and calculated integral elastic scattering cross sections for ground state Ba atoms at $E_0 = 20$ eV. Cross sections corresponding to $\Delta M = 0$ are large, i.e. somewhat larger than for the ground state atoms. For the $\Delta M = \pm 1$ case, the values become about two orders of magnitude smaller than in the $\Delta M = 0$ case. Interestingly, the cross section values for the $\Delta M = \pm 2$ case are intermediate in magnitude as already discussed in connection with the differential cross sections. The good agreement between experiment and theory for the ground state gives further support for the CCC method.

It should be kept in mind that all laser geometry and polarization-related conclusions apply only to the in-plane laser arrangement.

**Table 4.** Summary of integral cross sections for Ba from the CCC calculations ($10^{-16}$ cm$^2$).

| | Impact energy (eV) | | |
|---|---|---|---|
| | 2.8 | 20.0 | 97.8 |
| ($^1$P$_1$–$^1$P$_1$) elastic | | | |
| $Q(1,1) = Q(-1,-1)$ | 119.27 | 37.02 | 18.08 |
| $Q(1,0) = Q(-1,0)$ | 1.97 | 0.70 | 0.054 |
| $Q(1,-1) = Q(-1,1)$ | 4.52 | 1.57 | 0.36 |
| $Q(0,1) = Q(0,-1)$ | 1.16 | 0.59 | 0.054 |
| $Q(0,0)$ | 89.05 | 29.20 | 14.71 |
| $Q(M_i = 0)$ | 91.37 | 30.39 | 14.82 |
| $Q(M_i = 1) = Q(M_i = -1)$ | 125.77 | 39.29 | 18.49 |
| $Q(M_f = 0)$ | 31.00 | 10.20 | 4.94 |
| $Q(M_f = 1) = Q(M_f = -1)$ | 41.65 | 13.06 | 6.16 |
| $Q(M_i = \pm 1$ coh.) | 118.48 | 43.83 | 17.97 |
| $Q(135^\circ, 0^\circ, 0^\circ)$ | 111.23 | 32.77 | 16.63 |
| $Q(135^\circ, 180^\circ, 0^\circ)$ | 112.91 | 31.92 | 16.86 |
| $Q(135^\circ, 0^\circ, \psi_m)$ | 113.65 | 36.46 | 17.08 |
| $Q(135^\circ, 180^\circ, \psi_m)$ | 114.77 | 35.89 | 17.23 |
| $Q$ | 114.30 | 36.36 | 17.26 |
| $Q_{CR}^{[2]} = \left(\frac{2}{3}\right)^{1/2} [Q(M=1) - Q(M=0)]$ | 8.70 | 2.33 | 1.00 |
| ($^1$S$_0$–$^1$S$_0$) elastic | | | |
| $Q(0,0) = Q$ CCC[a] ($E_0 = 22.2$ eV) | — | 29.4 | — |
| $Q$ Experiment[b] ($E_0 = 20.0$ eV) | — | $26.7 \pm 5.3$ | — |

[a] Fursa and Bray (1998).
[b] Wang *et al* (1994).

## 6. Elastic electron scattering by metastable $^{138}$Ba atoms

As a byproduct of our investigation we also obtained elastic scattering cross sections for metastable $^{138}$Ba atoms resulting from the radiative decay of the laser-excited $^1$P$_1$ atoms. Elastic scattering measurements, made with the laser-low arrangement, yielded $\left[I_{\mathrm{M}}^{\mathrm{el}}\right]_{\mathrm{L}}$ (equation (B4) in appendix B) which was found to be independent of the geometry and polarization within the limits of experimental error. We disregarded the small (less than 1%) modulation seen in this signal (figure 2(*c*)) because it is partly due to some $^1$P$_1$ species reaching the interaction region with the laser-low arrangement, and, to some small extent, may be due to the anisotropic nature of the cascade-populated metastable levels. Normalization of these intensities (for each $E_0, \theta$ case) was again achieved by determining the intensity ratio $\left[I_{\mathrm{M}}^{\mathrm{el}}\right]_{\mathrm{L}}/[I_{\mathrm{S-P}}]_{\mathrm{off}}$, obtained under identical experimental conditions (see steps (c) and (d) in section 2.2) and utilizing the known DCS$_{\mathrm{S-P}}$ values of Wang *et al* (1994). We have

$$\mathrm{DCS_M} = \frac{\left[I_{\mathrm{M}}^{\mathrm{el}}\right]_{\mathrm{L}}}{[I_{\mathrm{S-P}}]_{\mathrm{off}}} \mathrm{DCS_{S-P}} \frac{1}{[N_{\mathrm{M}}/N_{\mathrm{tot}}]_{\mathrm{L}}}. \tag{18}$$

The differential cross sections obtained by these procedures are associated with 6s5d $^3$D$_2$ and 6s5d $^1$D$_2$ atoms assumed to be isotropic in their magnetic sublevel populations. Other metastable species can be neglected under our experimental conditions, as confirmed by our energy-loss spectra. The relative concentration of these two species, resulting from the spontaneous radiative decay of the laser-excited $^1$P$_1$ atoms, is given by the branching ratio of

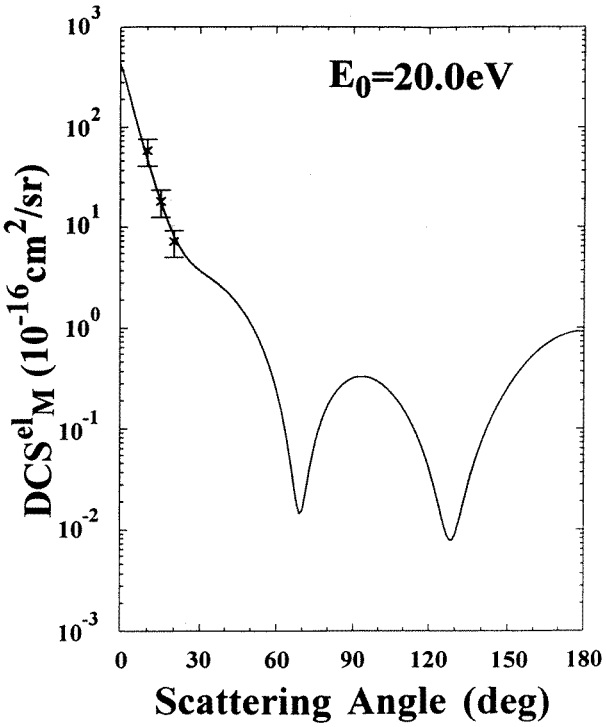


**Figure 10.** Elastic differential scattering cross sections for a mixture of 70% Ba(6s5d $^1D_2$) and 30% Ba(6s5d $^3D_2$) metastable atoms at $E_0 = 20$ eV. The full curve represents the CCC (115) results and the crosses with the error bars the experimental results (see text for further explanations).

$N_{^1D_2}/N_{^3D_2} = 2.3$, as measured by Bizzarri and Huber (1990). Thus

$$\mathrm{DCS_M} = 0.7\,\mathrm{DCS}_{^1D_2} + 0.3\,\mathrm{DCS}_{^3D_2}\,. \tag{19}$$

The results obtained from the present measurements for 20.0 eV at $\theta = 10^\circ, 15^\circ$ and $20^\circ$ are 57.8, 17.9 and $7.1 \times 10^{16}$ cm$^2$ sr$^{-1}$, respectively, with error limits of $\pm 30\%$. The non-relativistic CCC calculations yielded the values of $\mathrm{DCS_M}$ (defined by equation (19)) as shown in figure 10. We obtained the $\mathrm{DCS}_{^3D_2}$ values from the corresponding scattering amplitudes by angular momentum recoupling only. (A procedure which accounts for singlet–triplet mixing based on mixing coefficients yielded similar results.) The agreement between experiment and theory is good.

## 7. Plasma polarization spectroscopy

In plasma polarization spectroscopy, the polarization character of the radiation emitted by some component of the plasma is utilized to deduce information about local conditions in the plasma. The polarization associated with the emitted light is due to the polarization (alignment or orientation) of the atoms responsible for the radiation, which in turn is caused by the anisotropy of the excitation process. When the excitation is caused by electron impact, the presence of polarization in the emission is related to the anisotropic distribution of electrons. The relationship between the light polarization and the atomic polarization is well known, being based on quantum mechanical principles, but the relationships between the atomic polarization

and the anisotropy of the electron distribution for various systems has only recently been established (see, e.g., Kazantsev and Henoux 1995). These equations contain, as parameters, magnetic-sublevel-specific electron collision cross sections. One important parameter, which is of concern here, is the alignment creation cross section associated with elastic scattering, which is defined (Kazantsev *et al* 1988) as

$$Q_{CR}^{[2]} = \sum_{M} (-1)^{L-M} C_{LML-M} Q_M. \tag{20}$$

In our case, for the collision process

$$\mathrm{Ba}\big(\ldots 6s6p\ {}^1\mathrm{P}_1, \text{isotropic}\big) + \mathrm{e}(E_0) \rightarrow \mathrm{Ba}\big(\ldots 6s6p\ {}^1\mathrm{P}_1, \text{aligned}\big) + \mathrm{e}(E_0) \tag{21}$$

we have $Q_{CR}^{[2]} = \sqrt{\frac{2}{3}}[Q(M_f = 1) - Q(M_f = 0)]$.

The upper right index, [2], for $Q$ refers to the fact that $Q_{CR}^{[2]}$ is a second-rank alignment tensor in the expansion of the density matrix operator of the system (see Kazantsev and Henoux 1995 for details). $Q(M_f)$ is the integral elastic scattering cross section for process (21) with specific final magnetic sublevel quantum number $M_f$. Averaging over $M_i$ and the spin of the continuum electron is implied. It should be noted that the diagnostic species do not have to be a natural component of the plasma, and could be introduced as trace elements for this purpose. Ba has been used for such a purpose in the past.

The question has been raised recently as to whether elastic electron scattering can create alignment, and if so to what degree (Petrashen *et al* 1983, Dashevskaya and Nikitin 1987, Fujimoto 1996, Kazantsev 1996). The present study sheds some light on this question. From the integral $Q(M_f)$ values obtained from the CCC calculations, we derived the alignment creation cross sections listed in table 4. As may be seen, these cross sections are about a factor of five smaller than the $Q(M_f = 0)$ and $Q(M_f = 1)$ integral elastic scattering cross sections and are by no means negligible. To our knowledge no experimental cross section data of this type exist presently. Theoretical calculations could supply these cross sections, but their reliability must be checked against benchmark experiments. Our present effort is a step in this direction.

## Acknowledgments

This work was supported by the National Science Foundation, the National Aeronautics and Space Administration and the Department of Energy in the USA and by the South Australian Centre for High Performance Computing and Communications in Australia. One of us (LRL), wishes to thank the National Research Council for the Resident Research Associateship appointment. The authors wish to thank T Fujimoto and S A Kazantsev for calling our attention to the question raised in connection with the creation of alignment in elastic electron collisions and its importance in plasma polarization spectroscopy as well as for valuable discussions. We also wish to acknowledge valuable discussions with D C Cartwright and P W Zetner and the help of M B Das in preparing the manuscript.

## Appendix A. Determination of the target beam composition

Determination of the population fraction for the *laser-low case* needs to be considered first. The ground state population fraction (including all isotopes) is obtained from

$$\frac{[N_\mathrm{G}]_\mathrm{L}}{[N_\mathrm{G}]_\mathrm{off}} = \frac{[N_\mathrm{G}]_\mathrm{L}}{N_\mathrm{tot}} = [n_\mathrm{G}]_\mathrm{L} = \frac{[I_\mathrm{S-P}]_\mathrm{L}}{[I_\mathrm{S-P}]_\mathrm{off}}. \tag{A1}$$

Here $I$ refers to the electron scattering intensity (total signal minus background), the lower right index for $I$ indicates the scattering channel (S–P means the $^1S_0$–$^1P_1$ inelastic channel). The lower right index of the square bracket refers to the laser (L means the laser is on and the arrangement corresponds to the laser-low case, C means the laser is on with laser-centre case, and off means that the laser is turned off). $[N_G]_L$ is the number of ground state atoms in the scattering region in the laser-low case, $[N_G]_{off}$ is the number of ground state atoms in the scattering region when the laser is turned off, which is equal to the total number of atoms in the scattering region, $N_{tot}$, and $[n_G]_L$ is the ground state population fraction in the interaction region for the laser-low case. The total excited population fraction is given by

$$\frac{[N_{exc}]_L}{N_{tot}} = [n_{exc}]_L = 1 - [n_G]_L \tag{A2}$$

and we have

$$[n_{exc}]_L = [n_M]_L \tag{A3}$$

where $[n_M]_L$ is the metastable population fraction for the laser-low case.

For the *laser-centre case*, using the same notation, we have

$$[n_G]_C = \frac{[I_{S-P}]_C}{[I_{S-P}]_{off}} \tag{A4}$$

and

$$\frac{[N_{exc}]_C}{N_{tot}} = [n_{exc}]_C = 1 - [n_G]_C = [n_M]_C + [n_P]_C. \tag{A5}$$

Here $[n_P]_C$ is the population fraction of the $^1P_1$ atoms for the laser-centre arrangement. We determine $[n_P]_C$ from the $(^1P_1$–$^1S_0)$ superelastic and $(^1S_0$–$^1P_1)$ inelastic scattering intensities measured with laser geometry of $\theta_n = 135^\circ$, $\phi_n = 0^\circ$ and $180^\circ$, and $\psi = \psi_m = 35.3^\circ$ and from application of the principle of detailed balance applied to the conventional superelastic and inelastic differential cross sections. It can be shown that

$$\frac{[N_P]_C}{N_{tot}} = [n_P]_C = d\left\{\frac{[I_{P-S}(135^\circ, 0^\circ, \psi_m)]_C}{[I_{S-P}]_{off}} - \frac{[I_{P-S}(135^\circ, 180^\circ, \psi_m)]_C}{[I_{S-P}]_{off}}\right\} \tag{A6}$$

where

$$d = \frac{1}{2}\frac{g_P}{g_S}\frac{E_0^S}{E_0^S + \Delta E}\frac{\mathrm{DCS}_{S-P}\left(E_0^S\right)}{\mathrm{DCS}_{S-P}\left(E_0^S + \Delta E\right)}. \tag{A7}$$

$[I_{P-S}(\theta_n, \phi_n, \psi)]_C$ refers to the $(^1P_1$–$^1S_0)$ superelastic scattering intensity for the case when the $^1P_1$ state was prepared with the laser geometry and polarization indicated in parentheses. $\psi_m$ is the 'magic' polarization angle defined by $\cos 2\psi_m = \frac{1}{3}$, $g_P/g_S$ $(= \frac{1}{3})$ is the statistical weight ratio for the $^1P_1$ and $^1S_0$ levels, $E_0^S$ is the electron-impact energy in the superelastic experiment and $\Delta E$ is the energy loss corresponding to the $^1S_0$–$^1P_1$ excitation. For the present experiments, $d = 1.3495$. The two terms within parentheses in equation (A6) represent the azimuthal scattering asymmetry for the indicated laser geometries and polarization (normalized to the laser off inelastic signal).

The derivation of equation (A6) involves the following steps:

$$\frac{I^S_{P\to S}(135^\circ, \phi_n, 35.3^\circ)_C}{[I^{in}_{S\to P}]_{off}} = \frac{N_P^S\,\mathrm{DCS}(135^\circ, \phi_n, 35.3^\circ)}{N_S^{in}\,\mathrm{DCS}_{S\to P}} \tag{A8}$$

where $\phi_n = 0^\circ$ or $180^\circ$ and it is assumed that the measurements were carried out under identical experimental conditions. We have $N_S^{in} = N_{tot}$, $N_P^S \equiv N_P$, and

$$2\,\mathrm{DCS}_P^{el} = \mathrm{DCS}_{P\to S}(135^\circ, 0^\circ, 35.3^\circ) + \mathrm{DCS}_{P\to S}(135^\circ, 180^\circ, 35.3^\circ) \tag{A9}$$

where $\mathrm{DCS}_{\mathrm{P}}^{\mathrm{el}}$ is the $^1\mathrm{P}_1$–$^1\mathrm{P}_1$ elastic differential scattering cross section for $^{138}$Ba averaged over initial and summed over final magnetic sublevel quantum numbers. The same designation was used for the DCSs as for the scattering intensities above. We assumed here that this value was the same for all isotopes and used the value obtained for the naturally occurring isotopic mixture by Wang *et al* (1994). Equation (A9) can be derived from the cross section modulation equations to be discussed later.

The detailed balance equation is

$$\mathrm{DCS}_{\mathrm{P}\to\mathrm{S}}^{\mathrm{S}}\left(E_0^{\mathrm{S}}\right) = \frac{g_{\mathrm{S}}}{g_{\mathrm{P}}}\left(\frac{E_0^{\mathrm{S}} + \Delta E}{E_0^{\mathrm{S}}}\right)\mathrm{DCS}_{\mathrm{S}\to\mathrm{P}}^{\mathrm{in}}\left(E_0^{\mathrm{S}} + \Delta E\right) \tag{A10}$$

where $g_{\mathrm{S}} = 1$ and $g_{\mathrm{P}} = 3$.

## Appendix B. Extraction of the elastic scattering intensity modulation associated with the $^{138}\mathrm{Ba}(^1\mathrm{P}_1)$ atoms

The measured (total) elastic scattering intensity modulation curve as shown in figure 2(*b*) contains several components:

$$[I_{\mathrm{tot}}(\psi)]_{\mathrm{C}} = \left[I_{\mathrm{B}} + I_{\mathrm{G}}^{\mathrm{el}} + I_{\mathrm{M}}^{\mathrm{el}} + I_{\mathrm{cP}}^{\mathrm{el}}(\psi)\right]_{\mathrm{C}} \tag{B1}$$

where $I_{\mathrm{B}}$, $I_{\mathrm{G}}^{\mathrm{el}}$, $I_{\mathrm{M}}^{\mathrm{el}}$ and $I_{\mathrm{cP}}^{\mathrm{el}}(\psi)$ denote the contribution from background, elastic scattering by ground, metastable and by coherently prepared $^1\mathrm{P}_1$ atoms, respectively. We are interested in the component associated with elastic scattering by the laser-excited $^{138}\mathrm{Ba}(^1\mathrm{P}_1)$ atoms. The other components, therefore, must be determined and subtracted from the total count rate. $I_{\mathrm{B}}$ is obtained from the count rate when the Ba beam is off. The ground state contribution is given as

$$\left[I_{\mathrm{G}}^{\mathrm{el}}\right]_{\mathrm{C}} = \left[I_{\mathrm{G}}^{\mathrm{el}}\right]_{\mathrm{off}}\frac{[N_{\mathrm{G}}]_{\mathrm{C}}}{[N_{\mathrm{G}}]_{\mathrm{off}}} = \left[I_{\mathrm{G}}^{\mathrm{el}}\right]_{\mathrm{off}}\frac{[N_{\mathrm{G}}]_{\mathrm{C}}}{N_{\mathrm{tot}}} = \left[I_{\mathrm{G}}^{\mathrm{el}}\right]_{\mathrm{off}}[n_{\mathrm{G}}]_{\mathrm{C}}. \tag{B2}$$

The metastable contribution is given as

$$[I_{\mathrm{M}}^{\mathrm{el}}]_{\mathrm{C}} = [I_{\mathrm{M}}^{\mathrm{el}}]_{\mathrm{L}}\frac{[n_{\mathrm{M}}]_{\mathrm{C}}}{[n_{\mathrm{M}}]_{\mathrm{L}}}. \tag{B3}$$

We obtain $[I_{\mathrm{M}}^{\mathrm{el}}]_{\mathrm{L}}$ from the intensity modulation curve with the laser-low arrangement. (It is actually constant, i.e. independent of $\psi$, as mentioned earlier.)

$$\left[I_{\mathrm{M}}^{\mathrm{el}}\right]_{\mathrm{L}} = \left[I_{\mathrm{tot}} - I_{\mathrm{B}} - I_{\mathrm{G}}^{\mathrm{el}}\right]_{\mathrm{L}} \tag{B4}$$

where

$$\left[I_{\mathrm{G}}^{\mathrm{el}}\right]_{\mathrm{L}} = \left[I^{\mathrm{el}}\right]_{\mathrm{off}}\frac{[N_{\mathrm{G}}]_{\mathrm{L}}}{[N_{\mathrm{G}}]_{\mathrm{off}}} = \left[I_{\mathrm{G}}^{\mathrm{el}}\right]_{\mathrm{off}}[n_{\mathrm{G}}]_{\mathrm{L}}. \tag{B5}$$

Combining equations (14) through (16) we have

$$\left[I_{\mathrm{M}}^{\mathrm{el}}\right]_{\mathrm{C}} = [I_{\mathrm{tot}}]_{\mathrm{L}} - [I_{\mathrm{B}}]_{\mathrm{L}} - \left[I_{\mathrm{G}}^{\mathrm{el}}\right]_{\mathrm{off}}[n_{\mathrm{G}}]_{\mathrm{L}}\frac{[n_{\mathrm{M}}]_{\mathrm{C}}}{[n_{\mathrm{M}}]_{\mathrm{L}}}. \tag{B6}$$

Now we can obtain from (12) the $\left[I_{\mathrm{cP}}^{\mathrm{el}}(\psi)\right]_{\mathrm{C}}$ modulation curve, the required population fractions having been obtained by the procedure described in appendix A.

## Appendix C. The normalization procedure

$\left[I_{\mathrm{cP}}^{\mathrm{el}}(\psi)\right]_{\mathrm{C}}$ curves obtained with various laser geometries represent the relative elastic differential scattering cross sections for $^{138}\mathrm{Ba}\left(^1\mathrm{P}_1\right)$ atoms prepared by laser excitation (with various laser geometries and polarizations at given $E_0, \theta$) or, equivalently, for $^{138}\mathrm{Ba}\left(^1\mathrm{P}_1\right)$ atoms with the corresponding magnetic sublevel superpositions. The normalization to the absolute scale was achieved by utilizing the $\left(^1\mathrm{S}\text{–}^1\mathrm{P}\right)$ inelastic differential scattering cross section (as measured by Wang *et al* (1994)), together with the ratio of the maximum of the $[I_{\mathrm{cP}}(\psi_{\max})]_{\mathrm{C}}$ modulation curve to the $\left(^1\mathrm{S}\text{–}^1\mathrm{P}\right)$ inelastic signal measured with laser off (but otherwise both under identical scattering conditions). We have

$$\frac{\left[I_{\mathrm{cP}}^{\mathrm{el}}(\psi_{\max})\right]_{\mathrm{C}}}{[I_{\mathrm{S-P}}]_{\mathrm{off}}} = \frac{\left[\,\mathrm{DCS}_{\mathrm{cP}}^{\mathrm{el}}\,\right]_{\max}}{[\mathrm{DCS}_{\mathrm{S-P}}]}\frac{[N_{\mathrm{P}}]_{\mathrm{C}}}{N_{\mathrm{tot}}} \tag{C1}$$

which yields $\left[\,\mathrm{DCS}_{\mathrm{cP}}^{\mathrm{el}}\,\right]_{\max}$ for the particular laser geometry (and $E_0, \theta$). The factors which normalize $\left[I_{\mathrm{cP}}^{\mathrm{el}}(\psi_{\max})\right]_{\mathrm{C}}$ to $\left[\,\mathrm{DCS}_{\mathrm{cP}}^{\mathrm{el}}\,\right]_{\max}$ also normalize the full modulation curve (for any $\psi$). The results of these manipulations are the $\mathrm{DCS}_{\mathrm{cP}}^{\mathrm{el}}(\psi)$ modulation curves for fixed laser geometry and $E_0, \theta$ values.

## Appendix D. Equations relating the EICPs and the cPs

The electron-impact coherence parameters (EICPs) and the collision parameters (cPs) are deduced from the same experimental results. It is obvious, therefore, that they are not an independent set of parameters. We presented both sets because they all have important physical meanings of their own. The formal relationships among these two sets of parameters can be derived in terms of the corresponding $g$-matrices by utilizing time-reversal symmetry relations. The required time-reversal symmetry relations for elastic electron scattering amplitudes have been derived by Bartschat (1989).

In a more pragmatic approach, one can write down the modulation equations both in terms of the forward and the inverse parameters at three laser geometries. The resulting three equations can then be solved to obtain either $\lambda$, $\cos\varepsilon$ and $h$ in terms of $p_1$, $p_2$ and $k$ or $p_1$, $p_2$ and $k$ in terms of $\lambda$, $\cos\varepsilon$, $h$ at given $E_0$ and $\theta$. (We have considered only three parameters instead of all four because $k$ and $h$ obtainable from the present type of experiments represent a combination of the third and fourth parameters.) The relations obtained from this approach are given as

$$\lambda = \frac{a}{b}$$

$$\cos\varepsilon = \frac{(p_1 - 1)p_2 - p_1 + a/b}{a/b - 1}$$

$$k = \frac{1}{\cos 2\theta}\left[\cos\theta\sin\theta(1 + p_1 + p_2 - p_1p_2) - h - 4\frac{a}{b}\cos\theta\sin\theta\right]$$

where

$$a = (p_2 - 1)p_2\sin^2\theta + p_1\left(1 + \cos^2\theta\right) - \sin^2\theta + \tan 2\theta[\sin\theta\cos\theta(1 + p_1 + p_2 - p_1p_2) - h]$$

$$b = 2\cos 2\theta + \tan 2\theta\sin\theta\cos\theta(4 - p_1 - p_2 + p_1p_2)$$

and

$$p_1 = \tfrac{1}{2}\left(c\sin^2\theta + 2\lambda - k\sin 2\theta\right)$$
$$p_2 = \frac{c\sin^2\theta - k\sin 2\theta - 2\cos\varepsilon + 2\lambda\cos\varepsilon}{c\sin^2\theta + 2\lambda - k\sin 2\theta - 2}$$
$$h = c\sin\theta\cos\theta - k\cos 2\theta$$

where

$$c = 1 - 3\lambda + \cos\varepsilon - \lambda\cos\varepsilon.$$

## References


Andersen N, Gallagher J W and Hertel I V 1988 *Phys. Rep.* **165** 1
Bartschat K 1989 *Phys. Rep.* **180** 1
Bauschlicher C W Jr, Jaffe R L, Langhoff S R, Mascarello F G and Partridge H 1985 *J. Phys. B: At. Mol. Phys.* **18** 2147
Bizzarri A and Huber M C E 1990 *Phys. Rev.* A **42** 5422
Bray I 1994 *Phys. Rev.* A **49** 1066
Brunt J N H, King G C and Read F H 1977 *J. Phys. B: At. Mol. Phys.* **10** 1289
da Paixao F J, Padial N T, Csanak G and Blum K 1980 *Phys. Rev. Lett.* **45** 1164
Dashevskaya E I and Nikitin E E 1987 *Sov. J. Chem. Phys.* **4** 1934
Fujimoto T 1996 Private communication
Fursa D V and Bray I 1997 *J. Phys. B: At. Mol. Opt. Phys.* **30** 5895
——1998 *Phys. Rev.* A **57** R3150
——1999 *Phys. Rev.* A **59** 282
Hall B V, Sang R T, Shurgalin M, Farrell P M, MacGillivray W R and Standage M C 1996 *Can. J. Phys.* **74** 97
Hanne G F, McClelland J J, Scholten R E and Celotta R J 1993 *J. Phys. B: At. Mol. Opt. Phys.* **26** L753
Hermann H W and Hertel I V 1982 *Z. Phys.* A **307** 89
Hermann H W, Hertel I V, Reinland W, Stomatovic A and Stoll W 1977 *J. Phys. B: At. Mol. Phys.* **10** 251
Hertel I V and Stoll W 1974a *J. Phys. B: At. Mol. Phys.* **7** 570
——1974b *J. Phys. B: At. Mol. Phys.* **7** 583
——1977 *Adv. At. Mol. Phys.* **13** 113
Karaganov V, Bray I, Teubner P J O and Farrell P M 1996 *Phys. Rev.* A **54** R9
Kazantsev S A 1996 Private communication
Kazantsev S A and Henoux J C 1995 *Polarization Spectroscopy of Ionised Gases* (Dordrecht: Kluwer)
Kazantsev S A, Polinovskaya N Ya, Pyatritskii L N and Edelman S A 1988 *Sov. Phys.–Usp.* **31** 785
Law M R and Teubner P J O 1995 *J. Phys. B: At. Mol. Opt. Phys.* **27** 2257
Li Y and Zetner P W 1994a *Phys. Rev.* A **49** 950
——1994b *J. Phys. B: At. Mol. Opt. Phys.* **27** L283
——1995 *J. Phys. B: At. Mol. Opt. Phys.* **28** 515
——1996 *J. Phys. B: At. Mol. Opt. Phys.* **29** 1803
Lin C C and Andersen W 1992 *Adv. At. Mol. Opt. Phys.* **29** 1
Macek J and Hertel I V 1974 *J. Phys. B: At. Mol. Phys.* **7** 2173
Masters A T, Murray A J, Pascual R and Standage M C 1996 *Phys. Rev.* A **53** 3884
McClelland J J, Lorentz S R, Scholten R E, Kelley M H and Celotta R S 1992 *Phys. Rev.* A **46** 6079
MacGillivray W R and Standage M C 1988 *Phys. Rep.* **168** 1
Moore C E 1949 *Atomic Energy Levels* (*NBS Circular No 467*) vol 1 (Washington, DC: US Govt Printing Office)
Niggli S and Huber M C E 1989 *Phys. Rev.* A **39** 3924
Petrashen A G, Rebane V N and Rebane T K 1983 *Opt. Spektrosk.* **55** 492
Register D F, Trajmar S, Csanak G, Jensen S W, Fineman M A and Poe R T 1983 *Phys. Rev.* A **28** 151
Register D F, Trajmar S, Jensen S W and Poe R T 1978 *Phys. Rev. Lett.* **41** 749
Sang R T, Farrel P M, Madison D H, McGillivray W R and Standage M C 1994 *J. Phys. B: At. Mol. Opt. Phys.* **27** 1187
Scholten R E, Shen G F and Teubner P J O 1993 *J. Phys. B: At. Mol. Opt. Phys.* **26** 987
Shi Z, Ying C H and Vuskovic L 1996 *Phys. Rev.* A **54** 480
Teubner P J O, Karaganov V, Law M R and Farrell P M 1996 *Can. J. Phys.* **74** 984

Trajmar S, Kanik I, Khakoo M A, LeClair L R, Bray I, Fursa D and Csanak G 1998 *J. Phys. B: At. Mol. Opt. Phys.* **31** L393
Trajmar S and Nickel J C 1992 *Adv. At. Mol. Opt. Phys.* **30** 45
Trajmar S and Register D F 1984 *Electron Molecule Collisions* ed I Shimamura and K Takayanagi (New York: Plenum) pp 427–93
Vuskovic L 1996 *Can. J. Phys.* **74** 991
Wang S, Trajmar S and Zetner P W 1994 *J. Phys. B: At. Mol. Opt. Phys.* **27** 1613
Zetner P W 1994 Private communication
Zetner P W, Li Y and Trajmar S 1993 *Phys. Rev.* A **48** 495
Zetner P W, Trajmar S and Csanak G 1990 *Phys. Rev.* A **41** 5980
Zetner P W, Trajmar S, Wang S, Kanik I, Csanak G, Clark R E H, Abdallah J Jr and Nickel J C 1997 *J. Phys. B: At. Mol. Opt. Phys.* **30** 5317
Zuo M T Y, Jiang T Y, Vuskovic L and Bederson B 1990 *Phys. Rev.* A **41** 2489